A mouse model of PTEN Hamartoma Tumour Syndrome reveals that loss of the nuclear function of PTEN drives macrocephaly, lymphoid overgrowth, and late-onset cancer

Priyanka Tibarewal[1,*], Victoria Rathbone[1], Sarah E Conduit[1], Gala Anastasia Electra Classen[1], Fiona Black[1], Mohammad Amin Danesh[1], Georgia Constantinou[1], Zeinab Asgarian[2], Koujiro Tohyama[3], Nisha Kriplani[4], Virginia Alvarez Garcia[4], Elizabeth Foxall[1], Djenat Belarbi[5,6,7], Marie Leverve[5,6,7], Wayne Pearce[1], Mahreen Adil[1], Zofia Varyova[1], Lucia Conde[1], Adriana Alves[1], Glenn R Masson[8], Roger L Williams[8], Adrienne M Flanagan[9, 10], Javier Herrero[1], Dr Isra Ahmed Mohamed[11] , Katerina Stroud[12], Marc Tischkowitz[12], Katherine Lachlan[13,14], Cheryl L Scudamore[15], Mark G H Scott[5,6,7], Nicholas R Leslie[4], Nicoletta Kessaris[2,*], Bart Vanhaesebroeck[1,*]

[1]Cancer Institute, University College London, UK
[2]Wolfson Institute of Biomedical Research, University College London, UK
[3]Department of Physiology, School of Dentistry, Iwate Medical University, Yahaba, Japan
[4]Institute of Biological Chemistry, Biophysics and Bioengineering, Heriot Watt University, Edinburgh, UK
[5]Université de Paris, 75014 Paris, France
[6]Institut Cochin, INSERM U1016, 75014 Paris, France
[7]CNRS, UMR8104, 75014 Paris, France
[8]MRC Laboratory of Molecular Biology, Cambridge, UK
[9]Research Department of Pathology, University College London, UK
[10]Cellular and Molecular Pathology, Royal National Orthopaedic Hospital, Stanmore, UK
[11]Cambridge University Hospitals NHS Foundation Trust, Cambridge, UK
[12]Department of Genomic Medicine, National Institute for Health Research Cambridge Biomedical Research Centre, University of Cambridge, Cambridge, UK
[13]Wessex Clinical Genetics Service, University Hospital Southampton, Princess Anne Hospital, Southampton, UK
[14]Human Development and Health, Faculty of Medicine, University of Southampton, Southampton, UK
[15]Exepathology, Exmouth, UK

*Corresponding authors

Author contributions: PT, NRL, NK and BV conceived the study, PT, VR, SEC, GAEC, FB, MAD, GC, ZA,KT, NK, VAG, EF, DB, ML,WP, MA, ZV, SH, LC, AA, GRM and MGHS performed and analysed the experiments, CLS performed the histological analysis, RLW, AMF and JH provided reagents/resources for the study, PT, NK and BV wrote the manuscript.

Competing interest statement: BV is a consultant for Pharming (Leiden, The Netherlands) and iOnctura (Geneva, Switzerland) and a shareholder of Open Orphan (Dublin, Ireland).

ABSTRACT

PTEN Hamartoma Tumour Syndrome (PHTS) is a rare disorder characterized by germline heterozygous mutations in the PTEN tumour suppressor gene, leading to multi-organ/tissue overgrowth, autism spectrum disorder and increased cancer risk. PHTS individuals display heterogeneity in phenotypes, which has been linked in part to the diverse genetic alterations in the *PTEN* gene and the multifaceted functions of this protein. Indeed, while PTEN primarily functions as a PIP_3 lipid phosphatase in the cytosol, regulating PI3K/AKT signalling, a pathway commonly

deregulated in cancer, it also plays crucial roles in maintaining chromosomal stability through nuclear activities such as double strand (ds) DNA damage repair. Recent studies have identified a subset of missense PHTS variants that cause nuclear exclusion of PTEN, impairing its nuclear functions. Here, we present our findings from one such pathogenic variant, *PTEN-R173C*, frequently found in PHTS and somatic cancers. Using cell biological and mouse modelling approaches, we show that PTEN-R173C has higher PIP_3 phosphatase activity than wild-type PTEN, resulting in effective regulation of canonical PI3K/AKT signalling. However, PTEN-R173C is unstable and excluded from the nucleus. Aligning with their near normal PI3K/AKT signalling, *Pten*$^{+/R173C}$ mice display a low incidence of solid tumours compared to *Pten*$^{+/-}$ mice. *Pten*$^{+/R173C}$ mice also exhibit lymphoid hyperplasia and macrocephaly which correlates with compromised nuclear functions of PTEN-R173C. That nuclear functions are compromised is demonstrated by reduced dsDNA damage repair in *Pten*$^{+/R173C}$ mice. Integrating PHTS patient data with findings from our mouse model, our study indicates that nuclear dysfunction of pathogenic *PTEN* variants is a key factor in predicting the onset of the different PHTS-associated phenotypes. We speculate that late-onset cancer in individuals with nuclear-excluded PTEN results from genetic alterations unrelated to PTEN itself, facilitated by impaired PTEN-mediated dsDNA damage repair.

KEY WORDS: PTEN, PI3K, PHTS, overgrowth, mouse model, cancer, macrocephaly, germline, ASD

INTRODUCTION

PTEN is a ubiquitously expressed tumour suppressor[1-3] that shows complete loss of expression in some cancers (e.g. prostate cancer and glioblastoma) and overrepresentation of missense variants in other tumours (e.g. endometrial cancer)[1,4]. Heterozygous germline variants in PTEN cause PTEN Hamartoma Tumour Syndrome (PHTS), a rare autosomal dominant disorder. A recent study puts the prevalence of PHTS as 1:8000-13,000[5] which is 10-20 fold higher than previous estimates[6]. Clinical features of PHTS include macrocephaly, developmental delay (DD), autism spectrum disorder (ASD), dermatological pathologies, gastrointestinal (GI) polyps, immune dysfunction, vascular anomalies. Individuals with PHTS also face a significantly increased risk of developing cancers particularly of the breast, endometrium and thyroid[7,8], with emerging evidence for ovarian cancer[9].

PTEN acts in both the cytosol and nucleus. Cytosolic functions of PTEN predominantly include lipid phosphatase activity on phosphatidylinositol(3,4,5)trisphosphate (PIP_3) and phosphatidylinositol(3,4)bisphosphate ($PI(3,4)P_2$), thereby antagonizing PI3K/AKT signalling[10]. PTEN also has protein-phosphatase activity, reducing phosphorylation of Ser/Thr/Tyr on proteins such as PTK6, DREBRIN, DVL2, FAK and SHC[11] , in addition to auto-dephosphorylating its T366 site[12]. Nuclear PTEN has been implicated in cell cycle control, dsDNA repair, maintenance of chromatin structure, genome integrity and transcriptional control[13,14].

The functional core of the PTEN protein consists of a catalytic (amino acids (AA) 16-185) and a C2 (AA 186-350) domain[15], with mutations in different regions differentially impacting PTEN expression and function. 65% of PHTS patients express *PTEN* variants such as deletions, DNA insertions or non-sense mutation leading to STOP codons (such as R130X and R233X) that result in PTEN truncation and are therefore predicted to cause heterozygous loss-of-expression. The remaining PHTS patients carry heterozygous missense mutations in the phosphatase or C2 domain, leading to expression of PTEN proteins with altered function or subcellular distribution[16,17]. These include mutations in the catalytic pocket resulting in loss of all catalytic activity [e.g. C124 (C124S/R), R130 (R130G/Q/L) and G129 (G129R)][15] or selective loss of PIP_3 phosphatase activity, while retaining protein phosphatase activity (e.g. G129E)[10]. Missense mutations leading to selective loss of protein phosphatase activity (Y138L/C)

96 have also been described, although these have not been reported in PHTS[12,18]. Recent reports have
97 shown that a subset of PTEN variants in PHTS (including K289E, D252G, F241S, I101T and others) are
98 excluded from the nucleus and therefore lack all PTEN nuclear functions[14].
99 The PIP_3 phosphatase activity of PTEN has long been regarded as the main and critical factor in
100 PHTS pathogenesis, yet other lipid phosphatase-independent functions of PTEN are now also emerging
101 as important[14]. Various studies have attempted to establish genotype-phenotype associations in PHTS.
102 Limited patient data make it challenging to ascertain the impact of individual variants in driving patient
103 phenotypes. This challenge has been partially overcome by classifying the variants based on their
104 position in the *PTEN* gene and their impact on PTEN expression and function[19-23]. Recently, a large
105 paediatric and adult patient cohort study revealed that missense variants are associated with early
106 disease onset, with DD and macrocephaly being the reason for early diagnosis, whereas *PTEN*
107 truncation variants are associated with late onset disease, with cancer being the reason for PHTS
108 diagnosis at later stages in life[16]. However, patient cohort studies have been limited by the variability
109 in age and sex of the individuals, one of the key challenges in rare disease research.
110 Genetically modified mice have helped overcome some of the challenges in PTEN research by
111 allowing assessment of PTEN functions in an endogenous tissue context[24]. They also serve as a
112 platform for testing potential treatments, such as PI3K pathway inhibitors, aimed at mitigating the
113 effects of PTEN loss. An example are mice with heterozygous loss of PTEN expression ($Pten^{+/-}$),
114 representing *PTEN* variants that result in loss of expression and function. This mouse model
115 recapitulates many aspects of human PHTS remarkably well in terms of cancer development and
116 lymphoid and brain overgrowth[25,26].
117 Here we report the creation and characterisation of a novel mouse model for PHTS, carrying a
118 PTEN-R173C (NM_000314.8(PTEN):c.517C>T (p.Arg173Cys)) missense variant in the germline. R173 is
119 located in the TI (Thr-Ile) loop in the catalytic domain of PTEN important for PTEN catalytic activity[15].
120 Mutation of R173 to Cys or His in similar ratios are observed in PHTS and sporadic cancers, with
121 conflicting reports on catalytic activity impact, from having been reported active to inactive[27-29]. R173
122 variants are frequently found in multiple patient cohort studies with 34 PHTS patients been reported
123 in literature to the best of our knowledge, and an additional four new patients identified with this
124 variant in the UK (**Supplementary Table 1**). Most patients with R173 variants received PHTS diagnosis
125 at young age due to presentation of macrocephaly, DD and cutaneous pathology. Adult patients
126 additionally presented with breast cancer, benign and malignant tumours of the skin, thyroid and
127 ovary, endometrial polyps and fibroids, GI polyps, with malignant disease onset much later in life (over
128 the age of 50 years). Vascular malformations, mainly haemangiomas, were also seen in adult patients
129 (**Table 1** and **Supplementary Table 1**).
130 Here, we first revisited the impact of the R173 mutation on PTEN expression and function using
131 biochemical and cell-based models, with a focus on PTEN-R173C. We show that PTEN-R173C has
132 reduced protein stability but retains its ability to dephosphorylate PIP_3 and therefore regulate the
133 canonical PI3K/AKT pathway in the cytosol. However, we find that this PTEN mutant is largely excluded
134 from the nucleus.
135 Several mouse models have been developed to distinguish the relative importance of the cytosolic
136 *versus* nuclear functions of PTEN (reviewed in[14]). For instance, $Pten^{m3m4}$ mice, engineered by Eng *et al.*,
137 feature non-naturally occurring PTEN mutations that result in a predominantly cytosolic PTEN
138 distribution without affecting its PIP_3 phosphatase activity. These mice have been extensively studied
139 for the impact of the nuclear-cytoplasmic partitioning of PTEN on neuronal and immune phenotypes,
140 although their tumour spectrum has not been reported[30-32]. Other models, expressing PTEN missense
141 variants found in PHTS such as F341V[33], and non-pathogenic mutations such as K13R, Y240F and
142 D384V[34,35], that do not affect the catalytic functions of PTEN but impact its nuclear/sub-cellular

localisation, have also been developed, but there is limited or no patient data for these individual variants (**Table 1** and **Supplementary Table 2**).

We created heterozygous germline *Pten*^{R173C} knock-in mice (*Pten*$^{+/R173C}$) as a unique model of a frequent pathogenic PHTS PTEN variant representing nuclear-excluded PTEN missense variants. We examined the consequences of this mutation on embryonic development, glucose metabolism, development of PHTS-relevant cancers as well as immune, neurological and behavioural phenotypes. By integrating our findings with phenotypic data from patients for this variant, and by comparison of reported data on the *Pten*^{m3m4} mice, we delineate the role of the nuclear functions of PTEN in the manifestation of PHTS phenotypes.

RESULTS

Increased PIP_3 phosphatase activity but reduced protein stability of PTEN-R173 mutant proteins upon transient expression in mammalian cells

Conflicting data on the catalytic activity of PTEN-R173 variants have been published. PTEN-R173 mutant proteins, expressed in *E. coli*, have been reported to be catalytically inactive[27] however, mutant PTEN proteins expressed in non-mammalian systems often fail to fold properly, resulting in lack of activity[17]. Consistent with this, in our hands, PTEN-R173C protein expressed in *E. coli* lacked *in vitro* PIP_3 lipid phosphatase activity (**Fig. S1**) and when expressed in Sf9 insect cells precipitated upon purification [36] (data not shown), rendering it unsuitable for use in *in vitro* assays.

A commonly used assay to determine the ability of PTEN and its mutants to regulate PI3K/AKT signalling involves transfection into the PTEN-null U-87 MG glioblastoma cell line (further referred to as U87) and assessment of basal AKT phosphorylation and cell proliferation[18]. Transient lentiviral expression of untagged PTEN-R173C in U87 revealed consistently lower expression levels compared to PTEN-WT (**Fig. 1A**, left panel), despite similar mRNA expression levels (**Fig. 1A**, right panel). Similar results were seen with PTEN-R173H, suggesting that other PTEN-R173 mutant proteins are less stable than PTEN-WT.

Expression of a dose range of PTEN proteins in U87 revealed that, compared to PTEN-WT, lower levels of PTEN-R173C or PTEN-R173H effectively downregulated AKT P-S473 and S6 P-S240/244 phosphorylation (**Fig. 1B**) and suppressed U87 proliferation (**Fig. 1C and S2A**). We also assessed the impact of PTEN-R173C expression in U87 cells on recruitment of a PIP_3-biosensor protein to the plasma membrane. In both serum-starved or insulin-stimulated cells, the biosensor plasma membrane to cytosol ratio (PM:cytosol) was significantly reduced upon treatment with the pan-class I PI3K inhibitor GDC-0941 or upon expression of PTEN-WT or PTEN-R173C, with the strongest decrease upon PTEN-R173C expression (**Fig. 1D and S2B**), despite its lower expression levels compared to PTEN-WT (**Fig. S2C**).

Taken together, these data suggest that in mammalian cells, PTEN-R173C is less stable but catalytically more active than PTEN-WT.

Evidence for a more open, proteolytically-sensitive protein conformation of PTEN-R173 mutants

We next investigated possible biochemical mechanisms underlying the reduced expression of PTEN-R173C mutants in U87 cells. Cycloheximide chase experiments of U87 cells transiently transfected with PTEN expression constructs indicated a reduced protein half-life of PTEN-R173C compared to PTEN-WT (**Fig. 1E, S3A** and Ref.[17]). A recent study has shown similar findings with PTEN-R173H[37].

PTEN protein stability and activity is regulated, in part, by phosphorylation on multiple C-terminal sites (S380/T382/T383/S385) by kinases such as CK2[38]. Such phosphorylation results in a more closed, less active and more stable protein conformation[38-42]. Upon transient expression of similar levels of untagged proteins in U87 cells, PTEN-R173C showed a ~50% lower level of S380/T382/T383 phosphorylation compared to PTEN-WT (**Fig. 1F**). Similar data were observed using YFP-tagged Rluc-PTEN-R173C and PTEN-R173H in HEK-293T cells (**Fig. S3B**), suggesting that reduced phosphorylation may contribute to the observed instability of PTEN-R173 mutants.

193 Dephosphorylation of S380/T382/T383/S385 on PTEN releases the inhibitory effect of these
194 phosphorylated residues on the C2 domain of PTEN, leading to a more open conformation with
195 increased membrane binding and therefore enhanced activity[38-41]. It has also been shown that, once
196 at the membrane, the active form of PTEN becomes degraded[43]. A study using computational
197 modelling predicted increased protein flexibility of PTEN-R173C/H mutants, leading to impaired
198 protein stability[29]. In order to gain insight into these phenomena, we used an intramolecular
199 bioluminescent resonance energy transfer (BRET)-based biosensor Rluc-PTEN-YFP in live HEK-293T and
200 PTEN KO HeLa cells. This biosensor reveals dynamic changes in PTEN conformational rearrangement
201 and function due to shifts in energy transfer between the donor/acceptor couple[44] (**Fig. S4A-B**). Using
202 this approach, PTEN-R173C and PTEN-R173H were found to be in a more open/flexible conformation
203 compared to PTEN-WT (**Fig. 1G**).
204 We previously reported that PTEN protein dephosphorylated on S380/T382/T383/S385 is more
205 prone to ubiquitination and degradation, and that this involves the K66 ubiquitination site in PTEN[43,45].
206 In line with this, when transiently expressed in U87 cells, the PTEN-R173C/K66R double mutant which
207 cannot be ubiquitinylated, showed increased protein expression levels compared to PTEN-R173C (**Fig.**
208 **1H**).
209 Altogether these data indicate that the PTEN-R173C protein has a more open conformation that
210 allows ubiquitination and degradation, leading to reduced protein levels.
211
212 **PTEN-R173 mutants are predominantly cytoplasmic and largely excluded from the nucleus**
213 The tumour suppressor functions of PTEN have been mostly attributed to its ability to regulate the
214 PI3K/AKT pathway, with the role of other PTEN functions such as protein phosphatase activity and
215 nuclear functions less well-studied in this context[13]. Given that our results so far show that PTEN-
216 R173C/H mutants are effective at regulating the PI3K/AKT pathway, we turned our attention to other
217 PTEN functions that might explain the high mutation frequency of this site in somatic cancers and
218 PHTS.
219 Analysis of the subcellular distribution of PTEN-R173C by transiently expressing C-terminally GFP-
220 tagged PTEN-R173C or PTEN-WT in Lenti-X™ 293T cells revealed a significantly lower
221 nuclear:cytoplasmic ratio of the GFP signal in cells expressing PTEN-R173C-GFP than in cells with PTEN-
222 WT-GFP, suggesting that PTEN-R173C was largely excluded from the nucleus (**Fig. 1I**). Nuclear
223 exclusion of the R173 mutants was also revealed upon expression of YFP-tagged Rluc-PTEN-WT, -
224 R173C or -R173H in HEK-293T or PTEN KO HeLa cells (**Fig. S5**).
225
226 **Homozygous germline PTEN-R173C expression is embryonically lethal in mice**
227 In order to study PTEN-R173C in its endogenous tissue context and to better understand its role in
228 PHTS, we created heterozygous germline *Pten*^{R173C} knock-in mice (*Pten*$^{+/R173C}$) by CRISPR-Cas9
229 technology (**Fig. S6**). Intercrosses of *Pten*$^{+/R173C}$ mice did not yield live-born homozygous *Pten*$^{R173C/R173C}$
230 mice (**Fig. 2A**). *Pten*$^{R173C/R173C}$ embryos were almost all reabsorbed at embryonic day (E)11.5, with
231 under-representation compared to Mendelian ratios at earlier time points (**Fig. 2A**). Intact
232 *Pten*$^{R173C/R173C}$ embryos were found up to E9.5 at which stage, 5 out of 9 embryos were smaller and had
233 not undergone turning, with the remaining 4 having been reabsorbed, suggesting that *Pten*$^{R173C/R173C}$
234 embryos die around E9.5 (**Fig. 2A**).
235 Given the embryonic lethality of homozygous *Pten* $^{R173C/R173C}$ mice, and the notion that PTEN
236 mutations in PHTS individuals are heterozygous, in the next series of experiments we used
237 heterozygous *Pten*$^{+/R173C}$ mice to further investigate the impact of the PTEN R173C mutation. For these
238 studies, we used littermate wild-type (*Pten*$^{+/+}$) mice as controls as well as *Pten*$^{+/-}$ mice, a well-
239 characterised model for PHTS[25,46-50].
240
241
242

243 **PTEN-R173C expressed from its endogenous promoter is unstable but retains PIP_3 phosphatase**
244 **activity**
245 As a cell-based model to study endogenous PTEN-R173C protein expression and function, we derived
246 mouse embryonic fibroblasts (MEFs) of the following genotypes: *Pten*$^{+/R173C}$, *Pten*$^{R173C/R173C}$, *Pten*$^{-/R173C}$
247 and compared these to *Pten*$^{+/-}$, *Pten*$^{-/-}$ and *Pten*$^{+/+}$ MEFs.
248 PTEN protein expression levels in *Pten*$^{+/R173C}$ and *Pten*$^{+/-}$ MEFs were 60-70% of those in *Pten*$^{+/+}$ MEFs
249 (**Fig. 2B**). The PTEN levels observed in *Pten*$^{+/-}$ MEFs agree with previous studies where the *Pten*^{WT} allele
250 was shown to express higher than 50% level of PTEN protein[51]. In *Pten*$^{R173C/R173C}$ and *Pten*$^{-/R173C}$ MEFs,
251 PTEN protein levels were ~13% and ~2%, respectively, of those in *Pten*$^{+/+}$ MEFs (**Fig. 2C**; **Fig. S7**),
252 indicative of low protein stability of the PTEN-R173C protein, in line with our exogenous expression
253 studies above.
254 We next used immunoblotting to assess PI3K pathway activation, under standard cell culture
255 conditions and upon insulin-stimulation. *Pten*$^{+/R173C}$, *Pten*$^{+/-}$ and *Pten*$^{+/+}$ MEFs growing in complete
256 media showed similar basal levels of phosphorylation of AKT, S6 and other downstream effectors (**Fig.**
257 **2B**). Under these conditions, *Pten*$^{-/-}$ MEFs had increased levels of AKT P-S473, which was not observed
258 in *Pten*$^{R173C/R173C}$ MEFs (**Fig. 2C**). In *Pten*$^{-/R173C}$ MEFs, the levels of AKT P-S473 were elevated compared
259 to *Pten*$^{+/+}$ and *Pten*$^{+/-}$ MEFs, but still substantially lower compared to *Pten*$^{-/-}$ MEFs (**Fig. S7**).
260 Upon insulin stimulation, the increase in AKT P-S473 was dampened more effectively in
261 *Pten*$^{R173C/R173C}$ MEFs than in *Pten*$^{+/+}$ and *Pten*$^{-/-}$ MEFs, despite the very low levels of PTEN-R173C
262 expression (**Fig. 2D**).
263 Taken together, these data indicate that, even at low levels of expression, PTEN-R173C is still
264 capable of effectively downregulating unstimulated and insulin-stimulated AKT P-S473
265 phosphorylation and thus retains overall PIP_3 phosphatase activity.
266
267 **PTEN-R173C regulates glucose metabolism *in vivo***
268 PTEN plays an important role in glucose metabolism by dampening insulin signalling, with *Pten*$^{+/-}$ mice
269 showing enhanced acute insulin signalling and increased glucose metabolism[52-54]. PHTS patients also
270 often show constitutive insulin sensitization[54]. In line with these reports, insulin tolerance tests on 3-
271 month-old mice revealed enhanced insulin sensitivity in *Pten*$^{+/-}$ mice, evidenced by lower levels of
272 blood glucose post insulin injection compared to WT littermates (**Fig. 2E**). In contrast, WT and
273 *Pten*$^{+/R173C}$ mice showed a similar insulin response up to 60 min after insulin injection (**Fig. 2E**). This
274 indicates that, at the organismal level, PTEN-R173C maintains the ability to downregulate acute
275 insulin/PI3K/AKT signalling and therefore glucose homeostasis (**Fig. 2E**).
276
277 **PTEN-R173C expressed from an endogenous promoter is predominantly nuclear-excluded with**
278 **reduced ability to regulate dsDNA damage repair**
279 To determine the subcellular distribution of PTEN-R173C upon expression from its endogenous locus,
280 we used immunocytochemistry and quantification of the PTEN nuclear/cytoplasmic ratio in
281 *Pten*$^{R173C/R173C}$ and *Pten*$^{-/R173C}$ MEFs. These data showed that PTEN-R173C expressed from its
282 endogenous locus was predominantly nuclear-excluded, in contrast to PTEN-WT protein which was
283 present in both the nucleus and cytoplasm (**Fig. 2F and S8A**). Given that R173 is not located in a known
284 PTEN nuclear localisation signal, one reason for the apparent nuclear exclusion of PTEN-R173C could
285 be sequestration at the plasma membrane, with little protein available for nuclear import. To
286 investigate this, we treated *Pten*$^{R173C/R173C}$ MEFs with the pan-class I PI3K inhibitor GDC-0941, with the
287 aim to reduce the PIP_3 substrate levels for PTEN at the plasma membrane and to potentially restore
288 the presence of PTEN-R173C in the nucleus. However, GDC-0941 treatment did not affect the
289 subcellular distribution of PTEN-R173C (**Fig. S8B**), suggesting that plasma membrane PIP_3 levels do not
290 significantly contribute to the nuclear exclusion of PTEN-R173C.
291 Nuclear PTEN has numerous functions including regulation of DNA repair, transcription, chromatin
292 structure, chromosomal stability and genome integrity by various mechanisms[13,14]. We investigated
293 one of these nuclear functions in *Pten*$^{+/R173C}$ mice, namely dsDNA repair. Nuclear PTEN deficiency has

294 been shown to cause a homologous recombination (HR) defect in cells, leading to increased γH2AX
295 expression and decreased Rad51 foci formation upon genotoxic stress such as ionizing radiation[55-57].
296 Ionizing radiation (IR) of *Pten*$^{+/R173C}$ and *Pten*$^{+/-}$ mice, followed by analysis 5 h post-IR treatment, led to
297 a similar increase in γH2AX levels in protein extracts from uteri, kidney and liver, compared to wild-
298 type mice (**Fig. 2G and S9**), indicative of a similarly reduced DNA repair capacity upon heterozygous
299 PTEN loss or heterozygous PTEN-R173C expression. This suggests that PTEN-R173C has a reduced
300 ability to regulate DNA damage repair compared to PTEN-WT.
301
302 **Reduced cancer predisposition of *Pten*$^{+/R173C}$ mice compared to *Pten*$^{+/-}$ mice**
303 Individuals with PHTS have an increased risk of cancers of multiple tissues including breast,
304 endometrium and thyroid[4,8,58]. To gain insight into the cancer predisposition of germline *Pten*^{R173C}
305 expression, we aged heterozygous *Pten*$^{+/R173C}$ mice alongside *Pten*$^{+/-}$ and *Pten*$^{+/+}$ littermate controls.
306 We used mice on a mixed C57Bl/6JxSv129 background, as on this background *Pten*$^{+/-}$ mice develop
307 PHTS-relevant phenotypes, with an overlapping tumour spectrum including hyperplasia/tumours of
308 the thyroid, endometrium, lymphoid tissue, small intestine and adenomyoepithelioma and malignant
309 mammary tumours in the females[26]. *Pten*$^{+/-}$ mice also develop lesions not seen in PHTS patients
310 including, pheochromocytoma and intraepithelial neoplasia (PIN) and adenocarcinoma of the
311 prostate[25,46-50].
312 Gross morphology and development of *Pten*$^{+/R173C}$ mice was found to be similar to *Pten*$^{+/+}$
313 littermates, with a tendency for a slight increase in body weight at young age in both *Pten*$^{+/R173C}$ and
314 *Pten*$^{+/-}$mice (**Fig. S10**).
315 Mice were aged and sacrificed at first appearance of signs of ill health or palpable masses. The
316 reasons for humane culling of mice are listed in **Supplementary Table 3**. Under these experimental
317 conditions, the median survival age of *Pten*$^{+/R173C}$ mice was 585 and 302 days for male and female mice,
318 respectively. This is significantly longer than the median survival age of 310 and 179 days for male and
319 female *Pten*$^{+/-}$ mice, respectively (**Fig.3A**). However, *Pten*$^{+/R173C}$ mice had a shorter lifespan compared
320 to wild-type mice (**Fig.3A**). This was especially the case for female *Pten*$^{+/R173C}$ mice, which were mainly
321 culled due to palpable masses or ill health.
322 Histopathological analysis of selected tissues from *Pten*$^{+/-}$ and *Pten*$^{+/R173C}$ mice revealed very similar
323 gross morphologies of all tissues analysed, with overall histopathology data summarized in **Fig. 3B** and
324 **Supplementary Tables 4-7.**
325 *Pten*$^{+/R173C}$ mice developed far fewer tumours than *Pten*$^{+/-}$ mice, with occasional hyperplasia of the
326 small intestine (2/14 mice) and low-grade PINs of prostate (4/14 mice), one case of mammary
327 adenocarcinoma (1/22 mice) and one case of endometrial hyperplasia (1/28) (**Fig. 3B; Fig. S11-S12;**
328 **Supplementary Tables 4 and 5**). Similar to *Pten*$^{+/-}$ mice, *Pten*$^{+/R173C}$ mice had a high incidence of
329 pheochromocytoma (**Fig. 3B, Fig. S11-S12; Supplementary Tables 4 and 5**).
330 One out of 28 *Pten*$^{+/R173C}$ mice displayed a single focus of endometrial hyperplasia, which correlated
331 with loss of immunostaining for PTEN and increased AKT P-S473 (**Fig. 3C**). Interestingly, loss of PTEN
332 immunoreactivity was also observed in microscopically *normal* endometrial glands from 5-month-old
333 and 10-month-old *Pten*$^{+/R173C}$ mice, but this was not accompanied by a concomitant increase in AKT P-
334 S473 immunoreactivity in these regions (**Fig. 3C**). In the absence of reagents which allow us to
335 specifically stain for WT or mutant PTEN protein and, based on the low expression level of endogenous
336 PTEN-R173C protein when expressed alone (**Fig. S7**), it is most likely that expression of the wild-type
337 *Pten* allele is lost in these morphologically normal glands. We speculate that, while the very low
338 expression level of PTEN-R173C from the endogenous allele may not be detectable by IHC, it is still
339 sufficient to partially downregulate PI3K signalling and AKT P-S473 and thereby prevent the
340 development of endometrial tumours. Although this observation is based on a single mouse, we
341 speculate that the hyperplastic gland found in the endometrium of this *Pten*$^{+/R173C}$ mouse may have
342 resulted either from loss-of-expression of the remaining *Pten*^{R173C} allele, or from acquisition of PI3K
343 pathway-activating mutations. These events likely led to PI3K pathway hyperactivation, ultimately
344 contributing to the development of endometrial hyperplasia. This hypothesis is supported by the fact

345 that somatic cancers with the PTEN-R173 mutation, along with mutation of the wild-type allele of
346 *PTEN*, also contain mutations in other cancer drivers such as *PIK3CA* (**Fig. 3D**).
347
348 **Prominent but delayed lymphoid hyperplasia in *Pten*$^{+/R173C}$ mice compared to *Pten*$^{+/-}$ mice**
349 Previous studies have reported a range of lymphoid and immune phenotypes in PHTS patients
350 including peripheral lymphoid hyperplasia, enlargement of tonsils and adenoids,
351 hypogammaglobulinemia, recurrent respiratory tract infection and autoimmune disorders.[59,60]. Some
352 of these phenotypes are found in a few PHTS patients with *PTEN*-R173 variants and other nuclear-
353 excluded variants (**Table 1** and **Supplementary Tables 1&2**).
354 In *Pten* mutant mice, lymphoid hyperplasia leads to enlarged cervical, brachial, inguinal and axillary
355 lymph nodes[25,51]. While this does not cause discomfort to the mice, in our study it was a main reason
356 for sacrificing *Pten*$^{+/-}$ mice (75% males and 80% females) and many *Pten*$^{+/R173C}$ mice (21% males and
357 50% females), due to animal welfare regulations on the allowed tissue overgrowth size
358 (**Supplementary Table 3**).
359 Histological analysis revealed a similar severity grade of hyperplasia (assessed by semi-quantitative
360 histopathological scoring) in female *Pten*$^{+/R173C}$ and *Pten*$^{+/-}$ mice but of significantly lower grade in
361 *Pten*$^{+/R173C}$ males than *Pten*$^{+/-}$ males (**Fig. 3E**). Lymphoid hyperplasia has also been reported in
362 heterozygous *Pten*$^{+/m3m4}$ mice[32].
363 Flow cytometry analysis of lymph nodes of 5-month-old female *Pten*$^{+/-}$ and 10-month-old female
364 *Pten*$^{+/R173C}$ mice, the age at which they have visibly enlarged lymph nodes, compared to littermate
365 *Pten*$^{+/+}$ mice, revealed a significant increase in the proportion of B-cells and a corresponding decrease
366 in T-cell proportions, a phenotype also reported in *Pten*$^{+/m3m4}$ mice (**Fig. 3F-G**).
367 Although we did not assess dsDNA damage repair in the lymphoid tissues of *Pten*$^{+/R173C}$ mice, the
368 lymphoid phenotypes correlate with loss of nuclear PTEN as this phenotype was also seen in *Pten*$^{+/m3m4}$
369 mice[32].
370
371 **Macrocephaly, increased neuronal complexity and white matter disturbances in *Pten*$^{+/R173C}$ mice**
372 PHTS patients, including the majority of patients with PTEN-R173 mutations (**Supplementary Table 1**),
373 commonly present with macrocephaly, DD and ASD. We therefore explored neurological and
374 behavioural phenotypes in *Pten*$^{+/R173C}$ mice.
375 We examined the brains and neurons from *Pten*$^{+/+}$, *Pten*$^{+/R173C}$ and *Pten*$^{+/-}$ mice and, where possible,
376 conditional knock-out mice that selectively lack PTEN expression in cortical pyramidal neurons
377 (referred to here as cKO)[61,62]. These cKO mice were further crossed with *Pten*$^{+/R173C}$ mice to obtain
378 conditional knock-in mice (referred to here as cKI) which express PTEN-R173C in cortical pyramidal
379 neurons without a copy of the PTEN-WT allele and are overall hemizygous for the *Pten*^{R173C} allele (*Pten*$^{-}$
380 $^{/R173C}$). The observed phenotypes are summarized in **Table 2**, which also shows a comparison to
381 phenotypes published for *Pten*$^{m3m4/m3m4}$ mice. The latter model germline expression of non-naturally
382 occurring PTEN mutations that leave PTEN PIP_3 phosphatase activity intact but lead to its nuclear
383 exclusion, and whose neuronal phenotypes have been extensively characterised[30-32].
384 We first assessed the levels of PTEN protein and downstream pathways in protein lysates from
385 cortical neurons. In the absence of a PTEN-WT allele, the level of PTEN protein in cKI was minimal and
386 similar to that seen in protein extracts of cKO mice (**Fig. S13A-B**). However, the level of AKT P-S473 in
387 cKI brains was significantly lower compared to the cKO mice (**Fig. S13A and C**). These observations
388 mirror our data in MEFs (**Fig. S7**), indicating that PTEN-R173C is also highly active in the brain despite
389 its low level of expression.
390 At 3 months of age, *Pten*$^{+/R173C}$ and *Pten*$^{+/-}$ mice of both sexes had enlarged brains with increased
391 mass compared to *Pten*$^{+/+}$ littermates (**Fig. 4A-B, left panel**). Whole-body mass was also increased in
392 both *Pten* mutant genotypes (**Fig. 4B, middle panel**), however, the brain was disproportionally
393 enlarged (**Fig. 4B, left panel**), indicating a macrocephalic phenotype. Also, at 3- and 6-months of age,
394 and independent of the genetic background, *Pten*$^{+/R173C}$ and *Pten*$^{+/-}$ mice showed a similar increase in
395 brain mass (**Fig. S14**). Given the apparently normal PI3K/AKT regulatory capacity of PTEN-R173C, and

396 the neurological phenotypes and macrocephaly previously observed in nuclear-excluded PTEN in
397 heterozygous *Pten*$^{+/m3m4}$ and homozygous *Pten*$^{m3m4/m3m4}$ mice[30,31], these observations allow us to
398 postulate that the nuclear function of PTEN is key to the development of macrocephaly.
399 We next quantified several brain parameters to characterize the macrocephalic phenotype in more
400 detail. *Pten*$^{+/R173C}$ mice had increased cortical thickness as measured at the level of the somatosensory
401 barrel field (**Fig. 4C-D**). A significant increase was also observed in the thickness of the corpus callosum
402 at four different Bregma levels (**Fig. 4E**) in both *Pten*$^{+/R173C}$ and *Pten*$^{+/-}$ mice. Consistent with
403 macrocephaly, a lengthwise enlargement of the corpus callosum as well as an increase in the total area
404 of this white matter tract at Bregma level were also observed (**Fig. 4F**). The increased thickness of the
405 cortex was not caused by increased NEUN+ neuronal cell numbers or neuronal densities (**Fig. 4G**). In
406 contrast, immunohistochemistry for OLIG2 revealed a small but significant increase in OLIG2-
407 expressing oligodendrocyte lineage cell numbers in the cortex of *Pten*$^{+/R173C}$ mice (**Fig. 4H**).
408 Interestingly, this increase was not seen in our *Pten*$^{+/-}$ mice and has not been reported in *Pten*$^{+/m3m4}$
409 mice but was observed in *Pten*$^{m3m4/m3m4}$ mice. Astrocyte overabundance and astrogliosis, as detected
410 by GFAP immunostaining, were not observed (**Fig. 4H**). Interestingly, astrogliosis has been reported in
411 *Pten*$^{m3m4/m3m4}$ mice, suggesting that the remaining wild type *Pten* allele protects the brain from this
412 immunoinflammatory phenotype.
413 To gain further insight into the causes of the macrocephaly, we quantified neuronal and glial
414 parameters *in vitro*. Morphologies of cortical pyramidal neurons *in vitro* were assessed following
415 transfection with a GFP expression vector to allow visualisation of the cells (**Fig. 5A**). *Pten*$^{+/R173C}$ neurons
416 had enlarged cell body size and increased process complexity compared to WT controls (**Fig. 5B,C**).
417 While cKO neurons demonstrated a more severe phenotype, this phenotype was not observed in
418 *Pten*$^{+/-}$ neurons and not reported in *Pten*$^{+/m3m4}$ mice but was observed in *Pten*$^{m3m4/m3m4}$ mice (**Fig. 5B,C**).
419 To determine whether glial and/or axonal defects contribute to the enlargement of the white
420 matter, we examined the corpus callosum of *Pten*$^{+/+}$, *Pten*$^{+/R173C}$ and *Pten*$^{+/-}$ mice using transmission
421 electron microscopy (**Fig. 5D**). We found a small increase in average axonal diameter in *Pten*$^{+/R173C}$
422 mice, with a reduction in the number of small diameter axons and a gain of larger diameter axons (**Fig.
423 5E**). This phenotype was not observed in *Pten*$^{+/-}$ mice. Quantification of the G-ratio in the corpus
424 callosum showed an increase in average myelin thickness in both *Pten*$^{+/R173C}$ and *Pten*$^{+/-}$ mice (**Fig. 5F**).
425 However, scatter plot analysis of the g-ratio as a function of axonal diameter did not show significant
426 changes in either *Pten*$^{+/R173C}$ and *Pten*$^{+/-}$ mice compared to controls (**Fig. 5G**).
427 Altogether, our experiments show that the macrocephalic *Pten*$^{+/R173C}$ phenotype is caused by
428 alterations in multiple parameters, including increases in neuronal cell body size, axonal thickness,
429 axonal complexity and oligodendrocyte lineage cell numbers.
430 *Pten*$^{+/R173C}$ mice have a similar degree of macrocephaly as *Pten*$^{+/m3m4}$ heterozygous mice and have
431 multiple neuronal phenotypes overlapping with *Pten*$^{m3m4/m3m4}$ homozygous mice and *Pten*$^{+/-}$ mice
432 (**Table 2**). Importantly, the apparently intact or even increased PI3K/AKT regulatory capacity of PTEN-
433 R173C, and the phenotypic overlap with *Pten*^{m3m4} mice, suggests that the nuclear function of PTEN is
434 key to the development of macrocephaly and several neuronal phenotypes.
435 Defective dsDNA damage repair is increasingly being associated with macrocephaly and ASD with
436 studies showing increased dsDNA breaks in cells isolated from patients with these phenotypes[63,64]. To
437 explore the possible involvement of impaired dsDNA damage repair in neurons in the macrocephalic
438 phenotype, we treated *Pten*$^{+/-}$ and *Pten*$^{+/R173C}$ mice with IR and examined the levels of γH2AX in the
439 brain 5 h post-IR treatment. While there was an increase in the γH2AX levels in protein extracts from
440 the brains of both *Pten*$^{+/-}$ and *Pten*$^{+/R173C}$ mice, compared to that seen in littermate wild-type mice, the
441 difference observed was not statistically significant (**Fig. S15**). This might be due to the IR dosage
442 and/or time of analysis, and warrants further investigation.
443
444 ***Pten*$^{+/R173C}$ mice display mild behavioural aberrations**
445 ASD is common in PHTS [4]. Behavioural abnormalities are found in mice with germline expression of
446 heterozygous loss-of-function of *Pten*[65] or homozygous expression of the nuclear-excluded *Pten*^{m3m4}

447 mutations[31]. To examine such type of aberrations in *Pten*$^{+/R173C}$ mice, we used a range of tests
448 associated with ASD-like mouse behaviours.
449 In Crawley's sociability test, *Pten*$^{+/R173C}$ mice were indistinguishable from *Pten*$^{+/+}$ littermate controls,
450 indicating normal social interactions (**Fig. S16A-D**). In the open field test, male mice were not
451 significantly different from their *Pten*$^{+/+}$ littermates with regards to distance travelled in the open field
452 arena and time spent moving during the test (**Fig. S17B,C**). However, female *Pten*$^{+/R173C}$ mice travelled
453 less and spent less time moving than WT controls (**Fig. S17F,G**), suggesting decreased exploratory
454 behaviour and/or decreased locomotion. This was not caused by increased anxiety since female (and
455 male) mice spent equal length of time exploring the different compartments of the open field test as
456 their WT controls (**Fig. S17D,H**), with defecation during the test being comparable between the two
457 groups (**Fig. S17E,I**). Reduced exploratory locomotion in females was also observed in a hole board
458 test (**Fig. S18A**). Changes in repetitive behaviours, as assayed in a marble burying test were absent in
459 both males and females (**Fig. S18B**).
460
461 **DISCUSSION**
462 Since the discovery of PTEN as a tumour suppressor in somatic cancer, multiple genetic mouse models
463 targeting *Pten* have been generated, highlighting the importance of PIP_3 phosphatase activity of PTEN
464 in tumour suppression, embryonic development, cellular homeostasis, neuronal development and the
465 development of autism spectrum traits[24].
466 PTEN mouse models have also improved our understanding of PHTS, a rare genetic condition
467 caused due to heterozygous germline *PTEN* mutations. These include *Pten*$^{+/-}$ mice which represent the
468 heterozygous genetic constellation of *PTEN* in PHTS and on a mixed C57BL6xSv129 background
469 develop multiple phenotypes overlapping with the clinical presentation of PHTS, including brain and
470 lymphoid overgrowth and the development of specific cancers[26]. While the PIP_3 phosphatase activity
471 of PTEN has been the focus of research over the last three decades, there is an increasing body of
472 evidence for other PTEN functions in disease pathogenesis, in particular its nuclear function[14].
473 Recently, the *Pten*^{m3m4} mouse model with germline expression of nuclear-excluded, engineered non-
474 naturally-occurring *Pten* mutations, has indicated a role for nuclear PTEN defects in driving neuronal
475 and immune phenotypes in PHTS[31,32].
476 In this study, we developed a new mouse model featuring the pathogenic PTEN-R173C variant
477 commonly found in PHTS and somatic cancer. We report that this PTEN variant retains its ability to
478 regulate PI3K/AKT signalling but is impaired in dsDNA damage repair through HR, likely due to nuclear
479 exclusion. Contrary to previous reports[27-29], we found that PTEN-R173 mutant proteins (R173C and
480 R173H) were catalytically more active PIP_3 lipid phosphatases than PTEN-WT, both in cells and tissues.
481 However, these mutants displayed reduced protein stability, possibly resulting from a more open
482 protein configuration that is more susceptible to ubiquitination-mediated degradation. Upon
483 heterozygous germline expression in *Pten*$^{+/R173C}$ mice, this biochemical feature results in PTEN protein
484 expression levels comparable to those in *Pten*$^{+/-}$ mice but an overall lipid phosphatase activity similar
485 to wild-type mice, as demonstrated by effective downregulation of insulin-stimulated PI3K/AKT
486 signalling.
487 *Pten*$^{+/-}$ mice with heterozygous PTEN loss are predisposed to a range of tumours similar to those
488 observed in PHTS patients[26]. To assess the importance of nuclear functions of PTEN in tumourigenesis,
489 we aged *Pten*$^{+/R173C}$ mice and found only a modest predisposition to solid tumour development
490 compared to *Pten*$^{+/-}$ mice. This is reminiscent of mouse models of genes involved in dsDNA damage
491 repair via HR such as *Brca*, *Rad51* and *Palb*[66-71]. Indeed, while homozygous inactivation of these genes
492 frequently leads to embryonic lethality, as also observed in *Pten*$^{R173C/R173C}$ mice, their heterozygous
493 inactivation only leads to a very low to absent tumour burden, most likely because the lifespan of mice
494 is insufficiently long to accumulate the additional mutations required for tumourigenesis[72]. That
495 additional genetic defects may be required to allow phenotypic output of PTEN-R173 defects is
496 indicated by the observation that somatic cancers with PTEN-R173 mutation have a range of co-
497 occurring mutations, including but not limited to oncogenic mutation in *PIK3CA* or loss of second allele

498 of *PTEN* (**Fig. 3D**). Also in mouse models, combination of *Pten* mutations with other oncogenic drivers
499 such as mutant *Pik3ca* and *ErbB2* have accelerated development of mammary tumours[73,74]. Combining
500 the *Pten-R173C* mutation in mouse models carrying additional cancer drivers (such as *PIK3CA*
501 mutation) or defects in DNA repair genes (such as *Brca* or *Rad51*) could provide evidence for this
502 speculation, but such experiments are outside the scope of the current study.
503 Our data further show that, in a germline configuration, deficient nuclear localisation of PTEN, and
504 consequently its nuclear function, correlates with brain and lymphoid overgrowth. While our study
505 does not establish a direct correlation between these overgrowth phenotypes in our mice and dsDNA
506 damage repair, it is possible that such a link exists. Indeed, one study reported increased IR-induced
507 DNA strand breaks in lymphocytes from autistic children compared to non-autistic controls supporting
508 such a functional link[64]. On the other hand, lymphoid cells isolated from PHTS patients with PTEN-
509 R173C mutation, who all present with ASD, did not exhibit increased DNA damage following IR
510 treatment compared to wild-type controls[75], suggesting that nuclear functions of PTEN other than
511 dsDNA repair may underlie the observed lymphoid overgrowth and macrocephaly in *Pten*$^{+/R173C}$ mice.
512 This is further supported by the absence of lymphoid overgrowth and macrocephaly in patients and
513 mouse models with germline mutations in other genes regulating dsDNA damage repair by HR, such
514 as the *Brca*, *Rad51* and *PalB2* genes.
515 We find that the macrocephalic *Pten*$^{+/R173C}$ phenotype correlates with alterations in multiple
516 parameters, including increases in neuronal cell body size, axonal thickness, axonal complexity and
517 oligodendrocyte lineage cell numbers. While this brain overgrowth phenotype in *Pten*$^{+/R173C}$ mice is
518 very clear, its impact on animal behaviour is less prominent. It has to be said that while mice with
519 heterozygous germline expression of PTEN accurately reflect the genetic makeup of patients with
520 PHTS, the behavioural abnormalities observed in heterozygous mutant mice are often subtle and
521 highly variable[65]. This necessitates large mouse numbers to achieve quantifiable significant differences
522 between genotypes. Consequently, the field of behavioural analysis has mostly relied on the use
523 homozygous mouse models. This approach is particularly true for PHTS, with numerous studies
524 conducted on homozygous brain-specific PTEN knockout models[76,77] and homozygous *Pten*^{m3m4}
525 models[31]. Similar homozygous models are also utilized in behavioural research on other rare diseases
526 such as Tuberous Sclerosis[78,79]. Although these models do not share the exact genetic composition of
527 patients, they serve as platforms for behavioural and neurological studies and testing therapeutics.
528 Our study suggests that the status of nuclear function of PTEN alongside its PIP_3 phosphatase
529 activity, allows refinement of genotype/phenotype analysis in PHTS. Based on our findings and
530 assessment of patient phenotypes (**Table 1** and **Supplementary Tables 1 and 2**), our data indicate that
531 individuals carrying *PTEN* variants such as *PTEN*^{R173C} that retain their PIP_3 phosphatase function but are
532 nuclear-excluded tend to follow a characteristic progression of known PHTS disease phenotypes: early-
533 signs such as neurological abnormalities – including macrocephaly and global developmental delay -
534 alongside cutaneous features which together lead to a PHTS diagnosis during childhood. As they enter
535 early adulthood, they may be prone to developing vascular abnormalities and benign tumours in the
536 thyroid and GI tract, with an increased likelihood of developing malignant cancers later in life.
537 Our study also highlights the possibility of new therapeutic treatments for cancer in PHTS patients.
538 A previous study has shown that glioma cells expressing PTEN-Y204F, a mutation that leads to lack of
539 PTEN nuclear localisation and functions such as dsDNA damage repair are more sensitive to radiation
540 therapy[35]. It is therefore tempting to speculate that radiation therapy and dsDNA damage repair
541 antagonist drugs, such as *PARP* inhibitors, might be additional therapeutic options beyond PI3K
542 pathway inhibitors for cancer in PHTS patients with R173 mutant-like PTEN variants.
543

544 **Methods**

545 **Plasmids**. DNA constructs are detailed in **Supplementary Table 8**. Point mutations were introduced in
546 PTEN WT cDNA in different vectors using primers listed in **Supplementary Table 9** and KOD hot start
547 DNA polymerase (Sigma-Aldrich) using the manufacturer's instructions.
548 **Mice.** All mice were maintained at University College London in accordance with the UK Animals
549 (Scientific Procedures) Act 1986 and following UK Home Office guidance. All procedures were
550 authorized by a UK Home Office Project Licence subject to local ethical review. *Pten*$^{+/-}$ mice [25],
551 *Pten*$^{flox/flox}$ mice [62], *CAG CreER*^{T2} mice [80] and *Emx1-Cre* mice [61] have been described elsewhere.
552 *Pten*$^{+/R173C}$ mice were generated by Taconic Biosciences using a CRISPR/Cas9 approach. gRNA was
553 designed to contain the R173C mutation (c.517C>T) and a silent mutation containing the *Eco*NI
554 restriction site upstream of the R173 site (to allow discrimination of wild-type and knock-in allele
555 following PCR). **Fig. S6** shows the gRNA sequence and the targeting strategy. gRNA was microinjected
556 into C57BL/6J mouse zygotes along with recombinant Cas9. The zygotes were then transferred to
557 pseudo-pregnant mothers. The litters born (founder animals) were sequenced to check for the
558 incorporation of the R173C mutation and percentage of mosaicism. They were then used to as a
559 breeder to generate F1 animals. F1 males positive for the R173C mutation and negative for any off-
560 target mutations were used to generate further animals by IVF using C57BL/6J females. All mouse lines
561 were maintained on a C57BL/6J background. Sv129 mice were purchased from Charles River or Envigo.
562 *Pten*$^{+/-}$ and *Pten*$^{+/R173C}$ mice were crossed with Sv129 mice to obtain mixed background F1 mice that
563 were used for some experiments as described. For neuronal studies, conditional knock-out mice that
564 selectively lack PTEN expression in cortical pyramidal neurons *were generated by crossing Pten*$^{flox/flox}$
565 mice with *Emx1-Cre* mice to give *Emx1-Cre*;*Pten*$^{fl/fl}$; referred to here as cKO. The cKO mice were crossed
566 with *Pten*$^{+/R173C}$ mice to obtain *Emx1-Cre*;*Pten*$^{fl/R173C}$,referred to here as cKI, which express one only
567 copy of *Pten*-R173C in the cortical pyramidal neurons.
568 For genotyping, mouse tissue samples (from ear biopsy or from the embryonic yolk sac) were lysed in
569 25 mM NaOH/0.2 mM disodium EDTA for 1 h at 95°C. The samples were neutralized by adding an
570 equal volume of a buffer containing 40 mM Tris-HCl, pH 4.5. Two µl of the DNA extract was used for
571 PCR using and Titanium polymerase PCR kit (Takara) and primers listed in **Supplementary Table 10**.
572 For genotyping of *Pten*$^{+/R173C}$ mice, an additional restriction digestion step was performed on the PCR
573 products using *Eco*NI (New England Biolabs).
574 **Mouse survival studies.** For sample size calculations for long term survival study, we use ClinCalc
575 (www.clincalc.com). The mean survival age of *Pten*$^{+/-}$ on a mixed C57BL6J x Sv129 background has been
576 reported to be 12±1.8 months [51]. The sample size required for *Pten*$^{+/R173C}$ mice needed to see a 15%
577 improvement in mean survival age compared to *Pten*$^{+/-}$ mice was calculated as 16 (probability of Type-
578 I error was set to 0.05 and Power was set to 80%). We used at least 16 mice for each genotype and
579 each sex. At least 10 Littermate wild type mice were used for both *Pten*$^{+/-}$ and *Pten*$^{+/R173C}$ mice. For
580 survival analysis, mice were weighed twice a week. They were monitored and euthanized upon
581 showing a more than 20% reduction in body weight, any signs of ill health such as hunched
582 appearance, laboured breathing, sluggish behaviour, or palpable masses with a total surface area of
583 1.4 cm^2 surface area. Animals showing no clinical signs were euthanized at the end of the study (600
584 days for females and 730 days for males).
585 **Cell lines.** U-87 MG (U87), HEK-293T and Phoenix cells were purchased from ATCC, Lenti-X™ 293T cells
586 were purchased from Clontech. Human PTEN knockout HeLa cell line and control HeLa cells was
587 obtained from Abcam (ab255419 and ab255928); PTEN knockout was validated using western blotting
588 (**Fig. S4C**). All cell lines were maintained in DMEM (Sigma-Aldrich), supplemented with 10% Filtered
589 Bovine Serum (FBS) (Pan-Biotech) and Pen-Strep (Sigma-Aldrich) using standard cell culture methods.
590 **Preparation of MEFs.** For preparation of E13.5 MEFs, timed matings were set up between *Pten*$^{+/-}$ mice
591 and *Pten*$^{+/R173C}$ mice, *Pten*$^{flox/+}$*CreER*^{T2} and *Pten*$^{+/-}$ or *Pten*$^{+/R173C}$ mice. Pregnant females were euthanized
592 on day 13.5 and embryos harvested from the uterus. Following removal of the head and visceral
593 organs, the rest of the embryo was minced in 2x Trypsin/EDTA using a sterile scalpel and incubated at
594 37°C for 40 min. The cell suspension was plated on 10 cm dishes in DMEM (Sigma-Aldrich) medium

595 supplemented with 10% FBS (Pan-Biotech) and Pen-Strep (Sigma-Aldrich), and cells maintained using
596 standard cell culture procedures. For preparation of E9.5 MEFs, timed intercrosses were set up
597 between *Pten*$^{+/R173C}$ mice. Pregnant females were euthanized on day 9.5, embryos removed from the
598 uterus and gently dissociated by pipetting up and down using a p1000 pipette and 2 ml of media
599 containing DMEM (Sigma-Aldrich), supplemented with 10% FBS (Pan-Biotech) and Pen-Strep (Sigma-
600 Aldrich). The cell suspension was plated in 48-well plates and cells maintained using standard cell
601 culture procedures. To induce Cre-mediated recombination of the floxed *Pten* allele in *Pten*$^{flox/+}$*CreER*^{T2}
602 MEFs, 4-hydroxy tamoxifen (Sigma Aldrich) was added to the cells at a final concentration of 1 µM and
603 refreshed every 24 h for 3 days.
604 **Primary neuron culture.** Primary cortico-hippocampal cultures were prepared from P1 or P2 pups
605 after genotyping. Cortex and hippocampus were dissected, digested with Trypsin, dissociated using
606 glass pipettes and 40,000 cells were plated per 12 mm coverslip. Neurons were cultured in serum-free
607 medium (neurobasal, NBA) medium supplemented with B27 supplement, L-glutamine,
608 penicillin/streptomycin and 10 mM HEPES pH 7.4. Cells were cultured at 5% CO_2 at 37°C with
609 replacement of half of the medium every 2-3 days. Cells were transfected on DIV6 with a GFP
610 expression vector using Lipofectamine 3000 according to the manufacturer's instructions. On DIV
611 12/13 cells were fixed with 4% PFA/4% sucrose in PBS for 10 min at room temperature (RT) and washed
612 3x in PBS. Cells were blocked and permeabilized in immunofluorescence (IF) buffer (PBS supplemented
613 with 0.3% Triton X and 3% BSA) for 20 min and incubated with primary antibodies to NeuN (Millipore
614 MAB377 and GFP, Abcam 1:1000) for 2 h at RT in IF buffer in a humidity chamber. After 3 washes with
615 PBS, cells were incubated with cross-absorbed Alexa Fluor labelled secondary antibodies (Invitrogen)
616 in IF buffer for 1 h at RT in a humidity chamber in the dark, washed 3x with PBS and mounted with
617 Immunomount. Neurons were imaged using a LSM 880 microscope (Leica) acquiring Z-stacks at 40 x
618 magnification. Dendritic complexity was determined using the Sholl macro in FIJI. Interceptions were
619 analysed in 10 µm radii within a 200 µm distance from the centre of the soma. To measure cell body
620 size in FIJI, stacks were processed to z-projections, ROIS were drawn manually around the cell bodies
621 and the ROI area was measured in FIJI.
622 **PTEN activity assays.** For purification of bacterially-expressed GST-tagged PTEN proteins, pGEX6P1
623 vectors with cDNA for WT or mutant PTEN were introduced in *E. coli* and recombinant PTEN was
624 purified by glutathione-affinity chromatography followed by cleavage of the GST tag as described [18].
625 PIP_3 assays using purified recombinant PTEN were performed with diC8 PIP_3 (Cell Signals Inc) and
626 malachite green phosphate assay kit (Sigma Aldrich) and have been described elsewhere [81].
627 Purification of recombinant PTEN protein from insect cells was as described in Ref.[82].
628 **Lentiviruses and retroviruses**. Lentiviruses for PTEN and PIP_3 biosensor were generated by co-
629 transfecting Lenti-X™ 293T cells or HEK-293T cells with plasmids expressing the cDNA of interest along
630 with packaging vectors using TransIT-LT1 following the manufacturer's instructions. For preparation
631 of retroviruses, Phoenix cells were transfected with p53 shRNA expressing vector [83] using TransIT-LT1
632 following the manufacturer's protocol. 24 h post transfection, sodium butyrate was added to the cells
633 to a final concentration of 12.5 mM for 6 h, followed by washing the cells with warm PBS and addition
634 of fresh media. The supernatant containing lentiviral particles was collected after 20 h, passed through
635 a 0.45 µm filter and stored at -80°C. Target-cells for transductions were plated at 40-50% confluency.
636 Once the cells had attached, lentiviral/retroviral particles were added to the cells along with polybrene
637 (Sigma-Aldrich) at 20 µg/µl. The media was changed 24 h post transduction.
638 **Immunoblotting analysis**. Protein extracts from cell cultures were prepared by scraping cells into lysis
639 buffer containing 25 mM Tris-HCl pH 7.4, 150 mM NaCl, 1% Triton X-100, 10% glycerol, 1 mM EGTA, 1
640 mM EDTA, 5 mM sodium pyrophosphate, 10 mM β-glycerophosphate, 50 mM sodium fluoride, 1 mM
641 sodium orthovanadate, 1 mM DTT and Protease inhibitor cocktail (Millipore). Mouse tissues harvested
642 from mice upon euthanasia were homogenize using Lysing Matrix M tubes (MP Biomedicals) in double
643 the volume (v/w) of lysis buffer (25 mM Tris-HCl pH 7.4, 150 mM NaCl, 1% Triton X-100, 0.1% SDS, 10%
644 glycerol, 1 mM EGTA, 1 mM EDTA, 10 mM sodium pyrophosphate, 20 mM β-glycerophosphate, 100
645 mM sodium fluoride, 2 mM sodium orthovanadate, 1 mM DTT and protease inhibitors) on a FastPrep

646 24 homogeniser (MP Biomedicals) at 4 m/sec for 20 sec. Cell or tissue lysates were pre-cleared by
647 centrifugation at 20,000xg for 10 min and protein extracts analysed by immunoblotting. 293T cells
648 expressing Rluc-PTEN-YFP constructs were lysed in buffer containing 50 mM HEPES (pH 7.4), 250 mM
649 NaCl, 2mM EDTA, 0.5% NP-40, 10% glycerol supplemented with protease and phosphatase inhibitors
650 (Roche) and protein A/G PLUS-Agarose (30µl/IP) and GFP antibody (Roche, Cat #11814460001, Mouse,
651 Dilution 1:200) was used to immunoprecipitate YFP-tagged PTEN protein which was used for
652 immunoblotting as described below. Protein gel electrophoresis was conducted with 10 µg of total
653 soluble protein per lane on NuPage Bis-Tris 4-12% gradient polyacrylamide gels (Thermofisher
654 Scientific) following the manufacturer's protocols. Proteins were transferred onto PVDF membrane
655 (Millipore) and membranes blocked in 5% milk powder/TBST for 1 h at RT. Blocked membranes were
656 incubated overnight with primary antibodies (**Supplementary Table 11**). Antibody complexes were
657 detected by 1 h incubation at RT with HRP-conjugated secondary antibodies (GE healthcare). Blots
658 were developed with Immobilon Forte Western HRP substrate (Millipore) and chemiluminescence
659 imaged using an ImageQuant LAS4000 imaging system (GE healthcare).
660 **qRT-PCR assays.** Total RNA was extracted from U87cells non-transduced or transduced with
661 lentiviruses for PTEN-WT, PTEN-C124S, PTEN-R173C or PTEN-R173H, using RNAEasy kit (Qiagen)
662 following the manufacturer's instructions. 1 µg of RNA was converted to cDNA using iScript RT kit
663 (BioRad). 50 ng of cDNA was used for QRT-PCR reactions using primers in **Supplementary Table 12**.
664 The reactions were run on a QuantStudio™ 5 Real-Time PCR machine (Applied Biosystems). dCT was
665 calculated by deducting the CT for GAPDH from CT of PTEN. ddCT was calculated by deducting the dCT
666 of untransduced cells from the dCT of the sample of interest.
667 **Cycloheximide chase studies.** U87 cells were transduced with lentiviruses for PTEN-WT, PTEN-C124S,
668 PTEN-R173C or PTEN-D252G. 48 h post transduction, cells were treated with 200 µg/ml cycloheximide,
669 lysed at different time points and protein extracts analysed for PTEN expression by immunoblotting.
670 **BRET assays.** BRET assays using the Rluc-PTEN-YFP biosensor were performed as described in Refs [44,84].
671 Briefly, 24 h post-transfection, cells were detached from 12-well plates, using trypsin-EDTA, and
672 resuspended in 1 ml of complete media. The cells were subsequently distributed into poly-L-ornithine-
673 coated (30 µg/ml) white 96-well optiplates (Perkin Elmer). The next day media was replaced with Opti-
674 MEM (Gibco) and Coelenterazine substrate (Interchim) was added to a final concentration of 5 µM
675 and incubated for 3 min at 25°C. BRET readings were then collected using a Multilabel Reader Mithras2
676 LB 943 (Berthold Technologies). Sequential integration of light output was measured for 1 sec using
677 two filter settings (480+10nm for YFP and 540+20nm for Rluc). The BRET signal represents the ratio of
678 the light emitted by YFP and the light emitted by Rluc (YFP/Rluc). The ratio values were corrected by
679 subtracting background BRET signals obtained with Rluc-PTEN. MilliBRET (mBRET) values were
680 calculated by multiplying these ratios by 1,000. Data are represented as specific mBRET values or
681 ΔmBRET when compared to the signal obtained with WT PTEN set to 0.
682 **MTS assays.** U87 cells were transduced with lentiviruses for GFP, PTEN-WT, PTEN-C124S, PTEN-R173C
683 or PTEN-R173H. 48 h post transduction, 5000 cells/well were plated in 96-well plates. A different plate
684 was prepared for each day. 20 µl of MTS assay reagent (Abcam) was added to the cells, incubated at
685 37°C for 1 h, followed by measurement of absorbance at 490 nm using a plate reader.
686 **PIP_3 biosensor analysis and PTEN localization using fluorescence microscopy.** For plasma membrane
687 PIP_3 quantification, U87-MG cells were transduced with lentiviral particles expressing the PIP_3
688 biosensor on its own or with lentiviral particles for PTEN-WT or PTEN-R173C, were pretreated ± GDC-
689 0941 (1 µM) for 1 h and stimulated ± insulin (100 nM) for 2 min. For PTEN localization studies, MEFs
690 were treated ± GDC-0941 (1 µM) 1 h prior to fixation. For both plasma membrane PIP_3 quantification
691 and localization of untagged or endogenous PTEN, cells were fixed with 4% PFA for 20 min, washed in
692 PBS, permeabilized with 0.1% Triton X-100 in PBS for 90 sec, washed 3 times with PBS and blocked
693 with PBS containing 1 or 3% (w/v) BSA for 30 min. Primary antibodies to PTEN were diluted in 1 or 3%
694 BSA block solution and incubated for 1 h at RT. Following 3 washes with PBS, secondary antibodies and
695 Phalloidin were diluted in 1 or 3% BSA block solution and incubated for 45 min at RT. Cells were then
696 washed 3 times and mounted using ProLong Gold antifade reagent containing DAPI (P36935, Life

697 Technologies). To examine GFP-PTEN localization during different stages of the cell cycle, Lenti-X™
698 293T cells were transfected with DNA for PTEN-WT-GFP or PTEN-R173C-GFP. 18 and 36 h post
699 transfection, culture medium was changed to fresh media containing 2 mM thymidine (Sigma). 18 h
700 post the second media change, the cells were released from double thymidine block by changing into
701 fresh, complete media. Cells were fixed with 4% PFA for 15 min, washed in 3 times in PBS and
702 permeabilized with 0.1% Triton X-100 in PBS for 5 min. Cells were then washed 3 times with PBS and
703 once with water before mounting using ProLong Gold antifade reagent containing DAPI. Confocal
704 microscopy was performed using a Zeiss LSM 880 microscope with AiryScan and a 63x PL APO objective
705 and Zen Black acquisition software or Zeiss LSM900 microscope and a 63x or 40x PL APO objective and
706 Zen Black acquisition software. Image processing was performed using Image J software (National
707 Institutes of Health, Rockville, MD, United States) and was limited to alterations of brightness,
708 subjected to the entire image. Quantification of plasma membrane PIP_3 intensity was performed using
709 Image J as described previously with minor modifications [85]. The average fluorescence intensity was
710 measured within a box of defined size (20 x 10 pixels) at three random regions of the plasma
711 membrane and three random regions of the cytosol (box size 20 x 20 pixels). The plasma membrane
712 and cytosol fluorescence intensity measurement were each averaged and the ratio of plasma
713 membrane to cytosolic fluorescence intensity determined. The PTEN nuclear to cytoplasmic ratio was
714 measured using Image J. First, the nuclear PTEN fluorescence intensity was measured, followed by the
715 cytoplasmic PTEN fluorescence intensity. The ratio of nuclear to cytoplasmic PTEN fluorescence
716 intensity was then calculated.
717 **Insulin tolerance test (ITT).** 3-month-old male *Pten*$^{+/-}$ and *Pten*$^{+/R173C}$ mice and their WT littermates
718 were starved for 6 h. The tip of the tail was punctured using a 26G needle and time-0 blood glucose
719 levels were recorded using a standard glucometer. The mice were given an IP injection of insulin to a
720 final concentration of 0.75 U/kg. Blood glucose readings were recorded at 15 min, 30 min, 45 min, 60
721 min, 90 min and 120 min post injection.
722 **Irradiation of mice:** 8-12-week-old mice were subjected to whole body irradiation of 7 Gy dose using
723 the Small Animal Radiation Therapy Platform (SARRP). 5 h post irradiation, the mice were euthanised
724 with a lethal injection of pentobarbital. Tissues of interest were harvested and snap frozen in liquid
725 nitrogen for biochemical analysis.
726 **Flow cytometry.** Mouse spleens and lymph nodes were mashed with a syringe plunger in RPMI
727 containing 10% FBS and filtered through a 70 µm filter. Cell suspensions from spleen were treated with
728 RBC lysis buffer (Biolegend). The cell suspensions were washed with PBS and stained with Fixable
729 Viability Dye eFluor™ 780 (ThermoFisher scientific) in PBS for 40 min followed by a few PBS washes.
730 For staining of surface antigens, antibodies were diluted in FACS staining buffer at 1:100 and added to
731 the cells for 30 min followed by two washes with FACS buffer. Details on antibodies and reagents used
732 is shown in **Supplementary Table 11**. The stained cells were analysed on BD FACSymphony™ analyser.
733 **Tissue processing for histological analysis and immunohistochemical analysis.** Mouse tissues were
734 fixed in 10% neutral buffered formalin for 24 h, followed by processing and embedding into paraffin
735 blocks. The tissues were orientated with the biggest surface down, to obtain complete sections. 3 µm
736 serial sections were cut and stained for Haematoxylin and Eosin, followed by immunohistochemistry
737 staining on the Leica BOND Rxm. Tissue sections for immunohistochemistry were incubated for 40 min
738 at 100°C in BOND epitope retrieval solution 2 (Leica, Germany), followed by blocking and staining using
739 the BOND polymer refine detection kit (Leica, DS9800), primary antibody (**Supplementary Table 11**)
740 and DAB enhancer (Leica, Germany).
741 **Histopathological analysis.** Non-neoplastic lesions, e.g. splenic extramedullary haematopoiesis and
742 lymph node hyperplasia, were graded using a standard semi-quantitative grading scheme from 0 to 5,
743 where 0 = lesion not present and 5 = the maximum lesion size/extent [86]. In general, where present,
744 the presence of other proliferative lesions including hyperplasia and neoplasia was recorded for each
745 individual organ, allowing the overall incidence to be established for each lesion in each group.
746 Prostatic intraepithelial neoplasia (PIN) was graded as low or high grade according to the consensus
747 suggested by Ittmann *et al.* [87]. Low-grade PIN lesions are focal, with one to two layers of cells and mild

748 nuclear atypia. High-grade lesions tend to be more extensive, filling the prostatic lumen but without
749 stromal invasion; have two or more cell layers often forming papillary or cribriform patterns; increased
750 nuclear atypia and mitoses.
751 **Perfusion and preparation of brain sections for DAB immunostaining and immunofluorescence.** Mice
752 were perfused with saline (0.9 % NaCl) followed by 4% PFA (w/v) in PBS through the left ventricle of
753 the heart. Brains were removed and post-fixed overnight at 4°C in 4% PFA, cryoprotected in 20%
754 sucrose in PBS for 24 h at 4°C and embedded in Tissue-Tek OCT compound (Sakura) in isopentane
755 cooled on dry ice. Frozen brains were stored at -80°C until use. Brains were processed on a Cryostat
756 (30 µm thickness) and sections were collected in PBS for immunohistochemistry. For DAB
757 immunostaining, floating sections were incubated with 0.3 % H_2O_2 in PBS for 30 min while shaking at
758 RT, and then blocked using blocking buffer (10% FBS in PBS supplemented with 0.1% Triton X-100) for
759 1 h at RT. After blocking, sections were incubated overnight at 4°C with primary antibodies diluted in
760 blocking buffer. Primary antibodies were detected with biotinylated secondary antibodies (Donkey
761 Anti-Mouse IgG Biotinylated Antibody, R&D systems) diluted 1:300 in blocking buffer for 1 h at RT. The
762 signal was amplified using the Vectastain ABC Kit HRP kit (Vector, PK-6100), according to the
763 manufacturer's instructions and developed using a DAB Peroxidase (HRP) Substrate Kit (Vector, SK-
764 4100) until the desired staining intensity was reached. Floating sections were mounted on Superfrost
765 plus slides in 0.2 % pork skin gelatine dissolved in 50 mM Tris-HCl pH 7.4, dried at RT overnight and
766 dehydrated in ethanol and xylene before mounting with DPX mounting medium (Merck). Images were
767 acquired using 20x magnification on a ZEISS Axio Scan.Z1 microscope and processed using ZEISS ZEN
768 lite software. For immunofluorescence, sectioned brains were blocked for 1 h before primary
769 antibodies were applied overnight. AlexaFluor 488 secondary antibody was used to detect OLIG2
770 (1:1000; Invitrogen, Carlsbad, CA) for 60 min at room temperature together with Hoechst 33258
771 (1:1000; Sigma) to detect cell nuclei. All secondary antibodies were diluted in block solution. Floating
772 sections were transferred onto Superfrost plus slides (BDH Laboratory Supplies) and air dried before
773 being coverslipped with Dako fluorescent mounting medium.
774 **Analysis of corpus callosum and cortex thickness and cell counting.** Matched sections at specified
775 Bregma levels were measured using the Zeiss Blue software measurement length tool. Counting boxes
776 were positioned onto matched slices in the barrel field of the primary somatosensory cortex
777 perpendicular to the corpus callosum. In each box, cells were counted from the border of the corpus
778 callosum to the pial surface. The length of the box was adjusted to fit the cortical thickness while the
779 width was not changed. All cells positive for NeuN within the box were counted and cell numbers
780 displayed as crude numbers in the box as well as density considering the area of the boxes analysed.
781 Four animals per genotype were used.
782 **Electron microscopy (EM).** EM was performed as described in Ref.[88]. Briefly, mice were prepared for
783 EM by PBS perfusion followed by 2.5% (v/v) glutaraldehyde and 2% (w/v) paraformaldehyde in 0.1 M
784 sodium cacodylate buffer (pH 7.6). Brains were removed and kept at 4°C for 48 h in the same fixative,
785 before being washed with 0.1 M cacodylate buffer, rinsed briefly with 0.1 M phosphate buffer and
786 shipped to Japan at ambient temperature. Sagitally-sectioned brains were processed for EM. After
787 immersion in a 1% (w/v) osmium tetroxide solution for 2 h at 4°C, the specimens were dehydrated
788 through a graded alcohol series and embedded in Epon 812 (TAAB Laboratories, UK). The required
789 area was trimmed, and ultrathin sections were cut, collected on a platinum-coated glass slide, stained
790 with uranyl acetate and lead citrate and imaged in a scanning electron microscope equipped with a
791 back-scattered electron beam detector (Hitachi SU8010) at 1.5 kV accelerating voltage. EM images of
792 sagittal sections of corpus callosum were taken at 15000x magnification. To estimate g-ratios, the
793 circumference of the axon and the external circumference of the myelin sheath were measured using
794 ImageJ, avoiding paranodal areas. The diameters of axon and myelin sheath were calculated from
795 these circumferential measurements, assuming a circular profile, and the g-ratio was calculated.
796 **Behavioural analysis.** Behaviour testing was carried out as previously described [89]. 12-week-old mice
797 on mixed C57BL/6 x Sv129 background were used in this study. All animals were kept on a 12 h light-
798 dark cycle with food and water accessible ad libitum. The indicated numbers of WT mice and their

Pten$^{+/R173C}$ littermates were tested in the open field test, three chambers test, hole board and marble burying. Mice tested in behavioural experiments were habituated to handling and the experimenter for 9 days before the start of behavioural experiments to reduce stress and habituated mice were generally handled by cupping. Mice were analysed in three cohorts and male and female mice were tested on separate days. During experiments white noise was played at around 50 Db to mask external noises and all experiments were video recorded. Before every experiment, mice were brought into the behavioural room 30 min before the first experiment for habituation and animals that had finished a test were transferred into a new cage in order not to influence the behaviour of the remaining experimental animals. Directly before the first experimental animal was tested and after every mouse the set up (open field, sociability chamber, hole board) was cleaned thoroughly with water and 70% ethanol in a consistent manner for every animal. Open field: the experimental animal was placed in an open field box measuring 30 cm x 30 cm. The walls were white and 40 cm high so that the animal could not get any visual clues. The mouse was allowed to roam freely for 30 min to explore the arena without any prior habituation. Distance, time spent in different areas and the time moving were analysed using Ethovision software while faecal boli were counted manually. Sociability: The experimental animal was placed into the central compartment of Crawley's chamber for 5 min with closed doors for habituation. After 5 min empty cages were placed into the middle of the left and right compartments and a stranger mouse was gently put into one of the cages (counterbalance left and right sides). The stranger mouse matched the subject mouse with regards to the breeding background, age and gender and had no contact with the subject mouse ever before. Both doors were opened at the same time and the experimental mouse was allowed to explore the area for 10 min. A stopwatch was used to determine the time the subject mouse spent closely interacting with either cage (direct contact/sniffing/cage climbing). The time spent with the empty cage versus the first stranger was measured, referred to as sociability. Calculation of discrimination indices: (time spent with mouse – time spent with empty cage)/(sum of the time spent with both). Hole board: since the experimental animals were familiar with the open field arena from the open field experiment, they were only briefly re-exposed to the empty arena for 10 min on day 1 of the hole board test. On the next day a hole board with 16 holes evenly spaced was placed into the arena, the subject mouse was put into the middle of the field and was recorded for 15 min. A manual cell counter was used to determine the total number of head dips into the holes. Marble burying: a cage was filled with 5cm of bedding that was tamped down lightly to produce an even surface. 12 glass marbles were distributed evenly spaced out in the cage and the animal was allowed to roam freely for 15 min. Marbles that were buried to 2/3 of their depth with bedding were counted.

Statistical analysis: GraphPad Prism (San Diego, CA, United States) was used for statistical analysis. The method used for individual datasets is indicated in the figure legends.

ACKNOWLEDGEMENTS. Personal funding was from the Jean Shanks Pathological Society (Clinical PhD fellowship; to V.R.), CRUK UCL Centre Non-Clinical Training Awards (C416/A29287 to G.C. and CANTAC721\100022 to F.B.) and the European Commission (H2020-MSCA-IF-2018 GA: 838559; to S.C.). Research in the B.V. laboratory was supported by PTEN Research (UCL-16-001, UCL-20-001), Cancer Research UK (C23338/A25722) and the UK Biotechnology and Biological Sciences Research Council (BB/W007460/1). Research in N.R.L. laboratory was supported by PTEN Research. Research in the M.G.H.S. group was supported by Fondation ARC pour la recherche sur le cancer (ARCPJA2022060005118) and Ligue Contre le Cancer (Comité de Paris). The UCL Cancer Institute Translational Technology Platforms are supported by the CRUK UCL Centre Award (C416/A25145). The N.K. lab is funded by grants from the UK Biotechnology and Biological Sciences Research Council (BB/N009061/1) and the Wellcome Trust (108726/Z/15/Z). M.T. and K.S. are supported by PTEN Research and the NIHR Cambridge Biomedical Research Centre (NIHR203312). The PHTS Patient Registry UK is funded by PTEN Research (UOC-17-001). G.R.M. and R.L.W. were supported by MRC funding (MC-A024-5PF91 to R.L.W.). We thank staff at the Technical Support Centre for Life Science Research in IMU for excellent technical support with EM processing. We also thank the UCL Research Capital Infrastructure Fund (RCIF) and the National Institute for Health Research University College London Hospitals Biomedical Research Centre for upgrade of the UCL Cancer Institute Microscopy facility and Dr Maria Whitehead and Dr Paul Elvin and members from the B.V. group for excellent feedback on the manuscript.

856 **REFERENCES**
857

858 1. Alvarez-Garcia, V., Tawil, Y., Wise, H.M. & Leslie, N.R. Mechanisms of PTEN loss in cancer: It's
859 all about diversity. *Semin Cancer Biol* **59**, 66-79 (2019).
860 2. Li, J. *et al.* PTEN, a putative protein tyrosine phosphatase gene mutated in human brain, breast,
861 and prostate cancer. *Science* **275**, 1943-7 (1997).
862 3. Steck, P.A. *et al.* Identification of a candidate tumour suppressor gene, MMAC1, at
863 chromosome 10q23.3 that is mutated in multiple advanced cancers. *Nat Genet* **15**, 356-62
864 (1997).
865 4. Yehia, L., Keel, E. & Eng, C. The Clinical Spectrum of PTEN Mutations. *Annu Rev Med* **71**, 103-
866 116 (2020).
867 5. White, S.L. *et al.* Population Prevalence of the Major Thyroid Cancer–Associated Syndromes.
868 *The Journal of Clinical Endocrinology & Metabolism* (2025).
869 6. Nelen, M.R. *et al.* Localization of the gene for Cowden disease to chromosome 10q22-23. *Nat*
870 *Genet* **13**, 114-6 (1996).
871 7. Ngeow, J. & Eng, C. PTEN in Hereditary and Sporadic Cancer. *Cold Spring Harb Perspect Med*
872 (2019).
873 8. Yehia, L. & Eng, C. 65 YEARS OF THE DOUBLE HELIX: One gene, many endocrine and metabolic
874 syndromes: PTEN-opathies and precision medicine. *Endocr Relat Cancer* **25**, T121-T140 (2018).
875 9. Schei-Andersen, A.J. *et al.* Non-serous ovarian cancer in PTEN Hamartoma Tumor Syndrome:
876 additional evidence for increased risk. *Fam Cancer* **24**, 28 (2025).
877 10. Myers, M.P. *et al.* The lipid phosphatase activity of PTEN is critical for its tumor supressor
878 function. *Proc Natl Acad Sci U S A* **95**, 13513-8 (1998).
879 11. Leslie, N.R., Maccario, H., Spinelli, L. & Davidson, L. The significance of PTEN's protein
880 phosphatase activity. *Adv Enzyme Regul* **49**, 190-6 (2009).
881 12. Tibarewal, P. *et al.* PTEN protein phosphatase activity correlates with control of gene
882 expression and invasion, a tumor-suppressing phenotype, but not with AKT activity. *Sci Signal*
883 **5**, ra18 (2012).
884 13. Ho, J., Cruise, E.S., Dowling, R.J.O. & Stambolic, V. PTEN Nuclear Functions. *Cold Spring Harb*
885 *Perspect Med* (2019).
886 14. Langdon, C.G. Nuclear PTEN's Functions in Suppressing Tumorigenesis: Implications for Rare
887 Cancers. *Biomolecules* **13**(2023).
888 15. Lee, J.O. *et al.* Crystal structure of the PTEN tumor suppressor: implications for its
889 phosphoinositide phosphatase activity and membrane association. *Cell* **99**, 323-34 (1999).
890 16. Hendricks, L.A.J. *et al.* Genotype-phenotype associations in a large PTEN Hamartoma Tumor
891 Syndrome (PHTS) patient cohort. *Eur J Med Genet* **65**, 104632 (2022).
892 17. Spinelli, L., Black, F.M., Berg, J.N., Eickholt, B.J. & Leslie, N.R. Functionally distinct groups of
893 inherited PTEN mutations in autism and tumour syndromes. *J Med Genet* **52**, 128-34 (2015).
894 18. Davidson, L. *et al.* Suppression of cellular proliferation and invasion by the concerted lipid and
895 protein phosphatase activities of PTEN. *Oncogene* **29**, 687-97 (2010).
896 19. Lachlan, K.L., Lucassen, A.M., Bunyan, D. & Temple, I.K. Cowden syndrome and Bannayan Riley
897 Ruvalcaba syndrome represent one condition with variable expression and age-related
898 penetrance: results of a clinical study of PTEN mutation carriers. *J Med Genet* **44**, 579-85
899 (2007).
900 20. Leslie, N.R. & Longy, M. Inherited PTEN mutations and the prediction of phenotype. *Semin Cell*
901 *Dev Biol* **52**, 30-8 (2016).
902 21. Marsh, D.J. *et al.* Mutation spectrum and genotype-phenotype analyses in Cowden disease
903 and Bannayan-Zonana syndrome, two hamartoma syndromes with germline PTEN mutation.
904 *Hum Mol Genet* **7**, 507-15 (1998).

905 22. Marsh, D.J. *et al.* PTEN mutation spectrum and genotype-phenotype correlations in Bannayan-
906 Riley-Ruvalcaba syndrome suggest a single entity with Cowden syndrome. *Hum Mol Genet* **8**,
907 1461-72 (1999).
908 23. Mighell, T.L., Evans-Dutson, S. & O'Roak, B.J. A Saturation Mutagenesis Approach to
909 Understanding PTEN Lipid Phosphatase Activity and Genotype-Phenotype Relationships. *Am J*
910 *Hum Genet* **102**, 943-955 (2018).
911 24. Lee, Y.R. & Pandolfi, P.P. PTEN Mouse Models of Cancer Initiation and Progression. *Cold Spring*
912 *Harb Perspect Med* **10**(2020).
913 25. Podsypanina, K. *et al.* Mutation of Pten/Mmac1 in mice causes neoplasia in multiple organ
914 systems. *Proc Natl Acad Sci U S A* **96**, 1563-8 (1999).
915 26. Tibarewal, P. *et al.* Long-term treatment of cancer-prone germline PTEN mutant mice with
916 low-dose rapamycin extends lifespan and delays tumour development. *J Pathol* **258**, 382-394
917 (2022).
918 27. Han, S.Y. *et al.* Functional evaluation of PTEN missense mutations using in vitro
919 phosphoinositide phosphatase assay. *Cancer Res* **60**, 3147-51 (2000).
920 28. Post, K.L. *et al.* Multi-model functionalization of disease-associated PTEN missense mutations
921 identifies multiple molecular mechanisms underlying protein dysfunction. *Nat Commun* **11**,
922 2073 (2020).
923 29. Smith, I.N. & Briggs, J.M. Structural mutation analysis of PTEN and its genotype-phenotype
924 correlations in endometriosis and cancer. *Proteins* **84**, 1625-1643 (2016).
925 30. Mester, J.L., Tilot, A.K., Rybicki, L.A., Frazier, T.W., 2nd & Eng, C. Analysis of prevalence and
926 degree of macrocephaly in patients with germline PTEN mutations and of brain weight in Pten
927 knock-in murine model. *Eur J Hum Genet* **19**, 763-8 (2011).
928 31. Tilot, A.K. *et al.* Germline disruption of Pten localization causes enhanced sex-dependent social
929 motivation and increased glial production. *Hum Mol Genet* **23**, 3212-27 (2014).
930 32. Jaini, R. *et al.* Germline PTEN mutations are associated with a skewed peripheral immune
931 repertoire in humans and mice. *Hum Mol Genet* **29**, 2353-2364 (2020).
932 33. Caserta, E. *et al.* Noncatalytic PTEN missense mutation predisposes to organ-selective cancer
933 development in vivo. *Genes Dev* **29**, 1707-20 (2015).
934 34. Igarashi, A. *et al.* Nuclear PTEN deficiency causes microcephaly with decreased neuronal soma
935 size and increased seizure susceptibility. *J Biol Chem* **293**, 9292-9300 (2018).
936 35. Ma, J. *et al.* Inhibition of Nuclear PTEN Tyrosine Phosphorylation Enhances Glioma Radiation
937 Sensitivity through Attenuated DNA Repair. *Cancer Cell* **35**, 504-518 e7 (2019).
938 36. Masson, G.R., Burke, J.E. & Williams, R.L. Methods in the Study of PTEN Structure: X-Ray
939 Crystallography and Hydrogen Deuterium Exchange Mass Spectrometry. *Methods Mol Biol*
940 **1388**, 215-30 (2016).
941 37. Jun, H.J. *et al.* Pleiotropic tumor suppressive functions of PTEN missense mutations during
942 gliomagenesis. *iScience* **27**, 111278 (2024).
943 38. Torres, J. & Pulido, R. The tumor suppressor PTEN is phosphorylated by the protein kinase CK2
944 at its C terminus. Implications for PTEN stability to proteasome-mediated degradation. *J Biol*
945 *Chem* **276**, 993-8 (2001).
946 39. Vazquez, F. *et al.* Phosphorylation of the PTEN tail acts as an inhibitory switch by preventing
947 its recruitment into a protein complex. *J Biol Chem* **276**, 48627-30 (2001).
948 40. Birle, D. *et al.* Negative feedback regulation of the tumor suppressor PTEN by
949 phosphoinositide-induced serine phosphorylation. *J Immunol* **169**, 286-91 (2002).
950 41. Odriozola, L., Singh, G., Hoang, T. & Chan, A.M. Regulation of PTEN activity by its carboxyl-
951 terminal autoinhibitory domain. *J Biol Chem* **282**, 23306-15 (2007).
952 42. Dempsey, D.R. *et al.* The structural basis of PTEN regulation by multi-site phosphorylation. *Nat*
953 *Struct Mol Biol* **28**, 858-868 (2021).

954 43. Maccario, H., Perera, N.M., Gray, A., Downes, C.P. & Leslie, N.R. Ubiquitination of PTEN
955 (phosphatase and tensin homolog) inhibits phosphatase activity and is enhanced by
956 membrane targeting and hyperosmotic stress. *J Biol Chem* **285**, 12620-8 (2010).
957 44. Lima-Fernandes, E. *et al.* A biosensor to monitor dynamic regulation and function of tumour
958 suppressor PTEN in living cells. *Nat Commun* **5**, 4431 (2014).
959 45. Gupta, A. & Leslie, N.R. Controlling PTEN (Phosphatase and Tensin Homolog) Stability: A
960 DOMINANT ROLE FOR LYSINE 66. *J Biol Chem* **291**, 18465-73 (2016).
961 46. Knobbe, C.B., Lapin, V., Suzuki, A. & Mak, T.W. The roles of PTEN in development, physiology
962 and tumorigenesis in mouse models: a tissue-by-tissue survey. *Oncogene* **27**, 5398-415 (2008).
963 47. Di Cristofano, A., Pesce, B., Cordon-Cardo, C. & Pandolfi, P.P. Pten is essential for embryonic
964 development and tumour suppression. *Nat Genet* **19**, 348-55 (1998).
965 48. Suzuki, A. *et al.* High cancer susceptibility and embryonic lethality associated with mutation of
966 the PTEN tumor suppressor gene in mice. *Curr Biol* **8**, 1169-78 (1998).
967 49. Freeman, D. *et al.* Genetic background controls tumor development in PTEN-deficient mice.
968 *Cancer Res* **66**, 6492-6 (2006).
969 50. Di Cristofano, A., De Acetis, M., Koff, A., Cordon-Cardo, C. & Pandolfi, P.P. Pten and p27KIP1
970 cooperate in prostate cancer tumor suppression in the mouse. *Nat Genet* **27**, 222-4 (2001).
971 51. Alimonti, A. *et al.* Subtle variations in Pten dose determine cancer susceptibility. *Nat Genet* **42**,
972 454-8 (2010).
973 52. Chen, C.Y., Chen, J., He, L. & Stiles, B.L. PTEN: Tumor Suppressor and Metabolic Regulator.
974 *Front Endocrinol (Lausanne)* **9**, 338 (2018).
975 53. Garcia-Cao, I. *et al.* Systemic elevation of PTEN induces a tumor-suppressive metabolic state.
976 *Cell* **149**, 49-62 (2012).
977 54. Pal, A. *et al.* PTEN mutations as a cause of constitutive insulin sensitivity and obesity. *N Engl J*
978 *Med* **367**, 1002-11 (2012).
979 55. Bassi, C. *et al.* Nuclear PTEN controls DNA repair and sensitivity to genotoxic stress. *Science*
980 **341**, 395-9 (2013).
981 56. Mendes-Pereira, A.M. *et al.* Synthetic lethal targeting of PTEN mutant cells with PARP
982 inhibitors. *EMBO Mol Med* **1**, 315-22 (2009).
983 57. Shen, W.H. *et al.* Essential role for nuclear PTEN in maintaining chromosomal integrity. *Cell*
984 **128**, 157-70 (2007).
985 58. Yehia, L., Ngeow, J. & Eng, C. PTEN-opathies: from biological insights to evidence-based
986 precision medicine. *J Clin Invest* **129**, 452-464 (2019).
987 59. Chen, H.H. *et al.* Immune dysregulation in patients with PTEN hamartoma tumor syndrome:
988 Analysis of FOXP3 regulatory T cells. *J Allergy Clin Immunol* **139**, 607-620 e15 (2017).
989 60. Drissen, M. *et al.* Increased frequency of infections and autoimmune disease in adults with
990 PTEN Hamartoma Tumour Syndrome. *Eur J Med Genet* **70**, 104960 (2024).
991 61. Kessaris, N. *et al.* Competing waves of oligodendrocytes in the forebrain and postnatal
992 elimination of an embryonic lineage. *Nat Neurosci* **9**, 173-9 (2006).
993 62. Lesche, R. *et al.* Cre/loxP-mediated inactivation of the murine Pten tumor suppressor gene.
994 *Genesis* **32**, 148-9 (2002).
995 63. Wang, M. *et al.* Increased Neural Progenitor Proliferation in a hiPSC Model of Autism Induces
996 Replication Stress-Associated Genome Instability. *Cell Stem Cell* **26**, 221-233 e6 (2020).
997 64. Attia, S.M. *et al.* Evaluation of DNA repair efficiency in autistic children by molecular
998 cytogenetic analysis and transcriptome profiling. *DNA Repair (Amst)* **85**, 102750 (2020).
999 65. Clipperton-Allen, A.E. & Page, D.T. Pten haploinsufficient mice show broad brain overgrowth
1000 but selective impairments in autism-relevant behavioral tests. *Hum Mol Genet* **23**, 3490-505
1001 (2014).
1002 66. Matos-Rodrigues, G., Martini, E. & Lopez, B.S. Mouse Models for Deciphering the Impact of
1003 Homologous Recombination on Tumorigenesis. *Cancers (Basel)* **13**(2021).

1004 67. Tsuzuki, T. *et al.* Targeted disruption of the Rad51 gene leads to lethality in embryonic mice.
1005 *Proc Natl Acad Sci U S A* **93**, 6236-40 (1996).
1006 68. Roy, R., Chun, J. & Powell, S.N. BRCA1 and BRCA2: different roles in a common pathway of
1007 genome protection. *Nat Rev Cancer* **12**, 68-78 (2011).
1008 69. Rantakari, P. *et al.* Inactivation of Palb2 gene leads to mesoderm differentiation defect and
1009 early embryonic lethality in mice. *Hum Mol Genet* **19**, 3021-9 (2010).
1010 70. Yan, D.H. *et al.* A delayed chemically induced tumorigenesis in Brca2 mutant mice. *Oncogene*
1011 **23**, 1896-901 (2004).
1012 71. Hakem, R. *et al.* The tumor suppressor gene Brca1 is required for embryonic cellular
1013 proliferation in the mouse. *Cell* **85**, 1009-23 (1996).
1014 72. Drost, R.M. & Jonkers, J. Preclinical mouse models for BRCA1-associated breast cancer. *Br J*
1015 *Cancer* **101**, 1651-7 (2009).
1016 73. Kato, T. *et al.* The Loss of Nuclear PTEN Increases Tumorigenesis in a Preclinical Mouse Model
1017 for Hepatocellular Carcinoma. *iScience* **23**, 101548 (2020).
1018 74. Yip, H.Y.K. *et al.* Control of Glucocorticoid Receptor Levels by PTEN Establishes a Failsafe
1019 Mechanism for Tumor Suppression. *Mol Cell* **80**, 279-295 e8 (2020).
1020 75. Wei, R. *et al.* Quantitative evaluation of DNA damage repair dynamics to elucidate predictors
1021 of autism vs. cancer in individuals with germline PTEN variants. *PLoS Comput Biol* **20**, e1012449
1022 (2024).
1023 76. Kwon, C.H. *et al.* Pten regulates neuronal arborization and social interaction in mice. *Neuron*
1024 **50**, 377-88 (2006).
1025 77. Zhou, J. *et al.* Pharmacological inhibition of mTORC1 suppresses anatomical, cellular, and
1026 behavioral abnormalities in neural-specific Pten knock-out mice. *J Neurosci* **29**, 1773-83
1027 (2009).
1028 78. Yuan, E. *et al.* Graded loss of tuberin in an allelic series of brain models of TSC correlates with
1029 survival, and biochemical, histological and behavioral features. *Hum Mol Genet* **21**, 4286-300
1030 (2012).
1031 79. Bateup, H.S. *et al.* Excitatory/inhibitory synaptic imbalance leads to hippocampal
1032 hyperexcitability in mouse models of tuberous sclerosis. *Neuron* **78**, 510-22 (2013).
1033 80. Schonhuber, N. *et al.* A next-generation dual-recombinase system for time- and host-specific
1034 targeting of pancreatic cancer. *Nat Med* **20**, 1340-1347 (2014).
1035 81. Maehama, T. & Dixon, J.E. The tumor suppressor, PTEN/MMAC1, dephosphorylates the lipid
1036 second messenger, phosphatidylinositol 3,4,5-trisphosphate. *J Biol Chem* **273**, 13375-8 (1998).
1037 82. Masson, G.R., Perisic, O., Burke, J.E. & Williams, R.L. The intrinsically disordered tails of PTEN
1038 and PTEN-L have distinct roles in regulating substrate specificity and membrane activity.
1039 *Biochem J* **473**, 135-44 (2016).
1040 83. Dickins, R.A. *et al.* Probing tumor phenotypes using stable and regulated synthetic microRNA
1041 precursors. *Nat Genet* **37**, 1289-95 (2005).
1042 84. Misticone, S., Lima-Fernandes, E. & Scott, M.G. Rapid Detection of Dynamic PTEN Regulation
1043 in Living Cells Using Intramolecular BRET. *Methods Mol Biol* **1388**, 95-110 (2016).
1044 85. Ooms, L.M. *et al.* The Inositol Polyphosphate 5-Phosphatase PIPP Regulates AKT1-Dependent
1045 Breast Cancer Growth and Metastasis. *Cancer Cell* **28**, 155-69 (2015).
1046 86. Scudamore, C. Practical approaches to reviewing and recording pathology data. in *A Practical*
1047 *Guide to Histology of the Mouse* (ed. C.L., S.) 25-42 (Wiley-Blackwell, Chichester, UK, 2014).
1048 87. Ittmann, M. *et al.* Animal models of human prostate cancer: the consensus report of the New
1049 York meeting of the Mouse Models of Human Cancers Consortium Prostate Pathology
1050 Committee. *Cancer Res* **73**, 2718-36 (2013).
1051 88. Kougioumtzidou, E. *et al.* Signalling through AMPA receptors on oligodendrocyte precursors
1052 promotes myelination by enhancing oligodendrocyte survival. *Elife* **6**(2017).
1053 89. Magno, L. *et al.* Transient developmental imbalance of cortical interneuron subtypes presages
1054 long-term changes in behavior. *Cell Rep* **35**, 109249 (2021).

1055
1056

1057

1058 **Table 1**

		PHTS patients with *PTEN* R173 variants	PHTS patients with other nuclear excluded *PTEN* variants	Both groups combined
Patient demographics	Number of patients (N)	34	25	59
	Age range (median age)	7mo-63y (12.5y)	1y-40y (6y)	7mo-63y (10y)
	Gender distribution N (%)	m: 19 (56%) f: 14 (41%) NR: 1 (3%)	m: 12 (48%) m: 9 (36%) NR: 4 (16%)	m: 31(52%) f: 23 (39%) NR: 5 (8%)
Phenotypes (N (%))				
Neuro-developmental	Macrocephaly	32 (94%)	21 (84%)	53 (90%)
	Developmental disorders	18 (53%)	16 (64%)	34 (58%)
Cutaneous and vascular features	Cutaneous pathology	16 (47%)	12 (48%)	28 (47%)
	Vascular abnormalities	5 (15%)	3 (12%)	8 (14%)
	Lipomas	-	4 (16%)	4 (7%)
	Malignant cancer of skin	1 (3%) Age: 63y	-	1 (1.7 %)
Immune/Lymphoid features	Various	3 (9%)	1 (4%)	4 (7%)
Thyroid	Benign lesions	6 (18%)	4 (16%)	10 (17%)
	Malignant cancer	1 (3%) Age: 59y	1 (4%) 29y	2 (3%)
Gastro-intestinal	Benign polyps	4 (12%)	5 (20%)	9 (15%)
Breast	Benign lesions	2 (6%)	1 (4%)	3 (5%)
	Malignant cancer	2 (6%) Ages: 54y & 59y	-	2 (3%)
Ovary	Benign lesions	3 (9%)	-	3 (5%)
	Malignant cancer	1 (3%) Age: 63y	-	1 (1.7 %)
Uterus	Benign lesions	3 (9%)	-	3 (5%)
Other cancers	Testicular cancer	-	1 (4%) Age: 29y	1 (1.7%)
	Lung cancer	-	1 (4%) Age: NR	1 (1.7%)

1059
1060
1061 **Table 1. Clinical phenotypes of PHTS patients with *Pten-R173* variants and other nuclear excluded**
1062 ***Pten* variants**
1063 mo, age in months; y, age in years; m, males; f, females, NR, not recorded. Phenotypic categories
1064 include the following: Developmental disorders; global developmental delay, delay in speech
1065 development, mental retardation, autism spectrum disorder, special educational needs. Cutaneous
1066 pathology; hamartomas, tricholemmoma, mucocutaneous lesions, acral keratoses, palmoplantar
1067 keratoses, oral papillomas, penile freckling, facial papules, café-au-lait spots, skin tags. Vascular

abnormalities; haemangiomas, venous malformations, arterio-venous malformations. Immune/ lymphoid features; recurrent upper respiratory tract infections, hypogammaglobulinemia, enlarged tonsils and adenoids, lymphadenopathy, splenomegaly. Thyroid benign lesions; cyst, nodules, adenomas. Thyroid malignant cancer; follicular cancer, papillary-follicular thyroid cancer. Breast benign lesions; fibrocystic disease of the breast, fibroadenomas, benign breast disease. Breast malignant cancer; ductal breast carcinoma, invasive ductal carcinoma and ductal carcinoma in-situ of the breast. Ovary benign lesions; ovarian cysts, benign neoplasm. Ovary malignant cancer; malignant neoplasm of the ovary. Uterus benign lesions; uterine fibroids, endometrial polyp. The phenotypes of individual patients are listed in Supplementary Tables 1 and 2.

1078 **Table 2**

Phenotypes	Mouse genotype				
	***Pten*$^{+R173C}$**	***Pten*$^{+/-}$**	***Pten*$^{-/-}$**	***Pten*$^{+/m3m4}$**	***Pten*$^{m3m4/m3m4}$**
Increased brain size	Yes	Yes	ND	Yes	Yes
Bigger corpus callosum	Yes	Yes	ND	ND	ND
Increased numbers of oligodendroglia cells	Yes	No	ND	No	Yes
Astrogliosis	No	No	ND	No	Yes
Increased cell body size	Yes	No	Yes	No	Yes
Increased neuronal complexity	Yes	No	Yes	No	No
Enlarged axons	Yes	No	ND	ND	ND
thinner myelin	Yes	Yes	ND	ND	ND
Sociability	No significant difference	ND	ND	No significant difference	Too social with revised criteria
Motor coordination	ND	ND	ND	ND	reduced
Locomotion	reduced	ND	ND	ND	ND

1079

1080 **Table 2. Neuronal and behavioural phenotypes in mice with *Pten* mutations**: Table shows data from
1081 *Pten*$^{+/R173C}$, *Pten*$^{+/-}$, and conditional *Pten*$^{-/-}$ mice from this study, and *Pten*$^{+/m3m4}$ *and* Pten$^{m3m4/m3m4}$ mice
1082 as reported in [30,31]. ND; not determined. The behavioural assays (sociability, motor coordination and
1083 locomotion) are relative to wild type littermate mice.

1084
1085

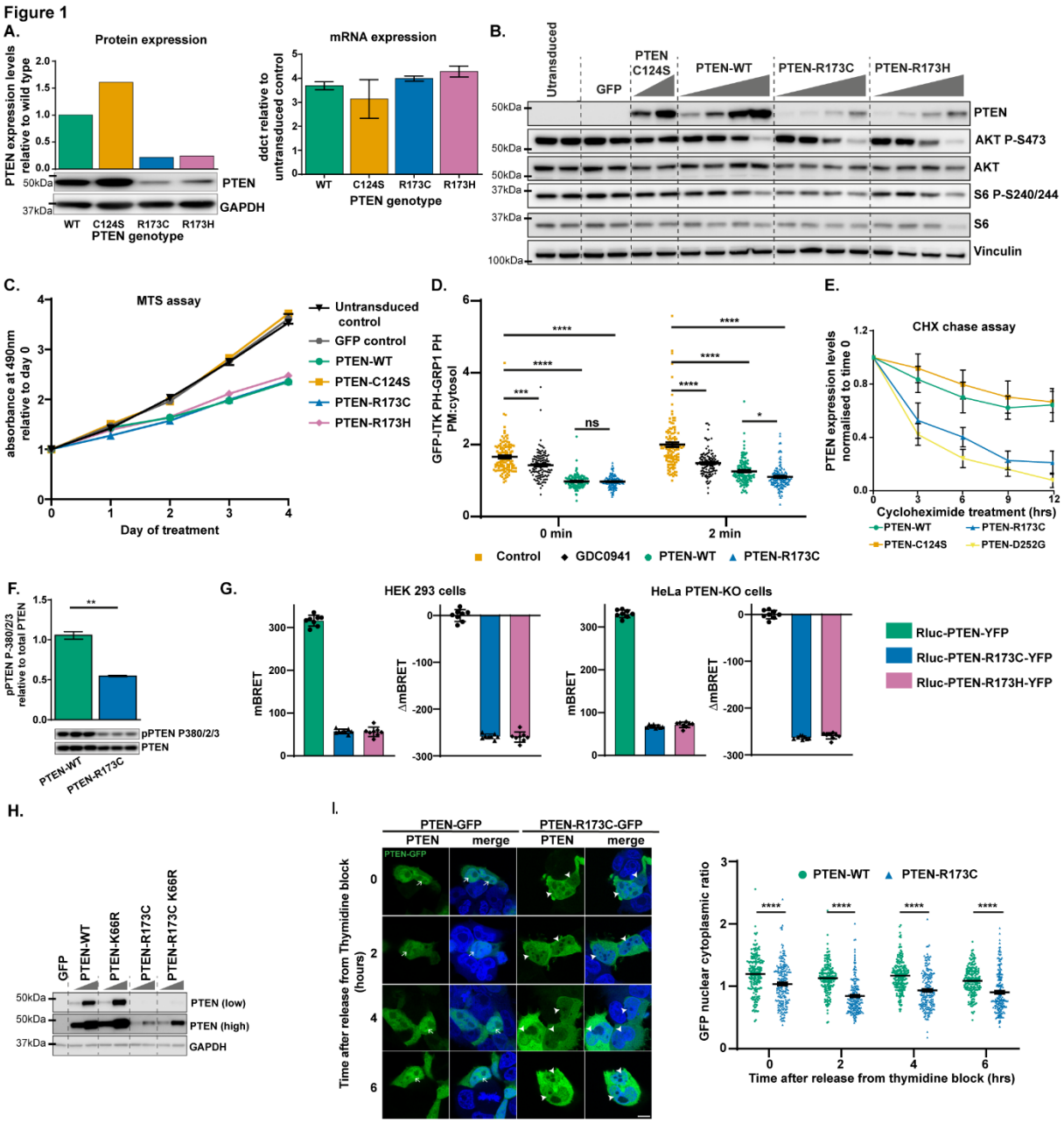

Figure 1. Characterisation of PTEN-R173C/H. (**A-C**) Transient lentiviral expression in U87 cells of PTEN-WT or the indicated PTEN mutants at fixed (A and C) or increasing concentrations of lentiviral particles (B). 48 h after transduction (A and B), cells were either lysed and PTEN expression and (B) AKT P-S473 and S6 P-S240/244 assessed by immunoblotting, or (A) qPCR analysis was performed to determine PTEN mRNA levels (mean ± SEM, n=3, right panel). The PTEN-C124S mutant was used as a control. (**C**) Cell proliferation was determined by MTS assay over 4 days. Graph shows the mean ± SEM of absorbance at 490 nm relative to day 0 from 10 replicate wells of a representative experiment from n=2. Immunoblots of PTEN protein and AKT P-S473 from the cells in (C) are shown in **Fig. S2A**. (**D**) U87 cells transduced with lentivirus expressing a PIP_3 biosensor, with or without PTEN-WT or PTEN-R173C, were pre-treated ± GDC-0941 (1 µM) for 1 h, followed ± insulin treatment (100 nM) for 2 min. The cells were stained with antibodies to PTEN and imaged by confocal microscopy (images in **Fig. S2B**). Graph shows mean fluorescence intensity (MFI) of the PIP_3 biosensor at the plasma membrane normalized to the MFI of the PIP_3 biosensor in the cytosol. Data shown as mean ± SEM from 3 independent experiments, statistical analysis performed using 2-way ANOVA. Representative immunoblots for PTEN protein and AKT P-S473 from the cells are shown in **Fig. S2C**. (**E-F**) Transient lentiviral expression

1103 of PTEN wild-type (WT) or the indicated PTEN mutants in U87 cells. (E) The cells were treated with
1104 cycloheximide and PTEN protein expression levels determined by immunoblotting at the indicated
1105 time points. Graph shows PTEN protein levels normalized to time 0, data shown as mean ± SEM, n=6.
1106 Representative blots shown in **Fig. S3A**. (F) Phosphorylation of PTEN on S380/T382/T383 was
1107 determined by immunoblotting. Quantification shows mean ± SEM, n=3, statistical analysis was
1108 performed using Unpaired Student's t-test. (**G**) mBRET and ΔmBRET values, obtained in live HEK-293T
1109 and HeLa PTEN KO cells, transfected with Rluc-PTEN-WT-YFP, Rluc-PTEN-R173C-YFP or Rluc-PTEN-
1110 R173H-YFP. Graphs represent mean ± SD of n=8 points from a representative experiment from 3
1111 independent experiments. (**H**) Transient lentiviral expression of PTEN-WT or the indicated PTEN
1112 mutants in U87 cells. Protein extracts from these cells were used for immunoblotting to assess PTEN
1113 protein levels. (**I**) Lenti-X™ 293T cells expressing GFP-tagged PTEN-WT or PTEN-R173C were arrested
1114 in the G1/S phase of cell cycle by double-thymidine block and imaged by confocal microscopy at the
1115 indicated time points after release from thymidine block, for expression of PTEN-GFP. Left panel shows
1116 representative images, arrows indicate nuclear PTEN-WT or reduced nuclear PTEN-R173C. Scale bar:
1117 10 µm. The graph shows the nuclear:cytoplasmic ratio of the mean fluorescence intensity (MFI) of the
1118 PTEN-GFP signal (mean ± SEM; n=3, statistical analysis performed using 2-way ANOVA). p-values for
1119 all statistical tests: *, $p< 0.05$; **, $p<0.01$; ***, $p<0.001$; ****, $p<0.0001$.

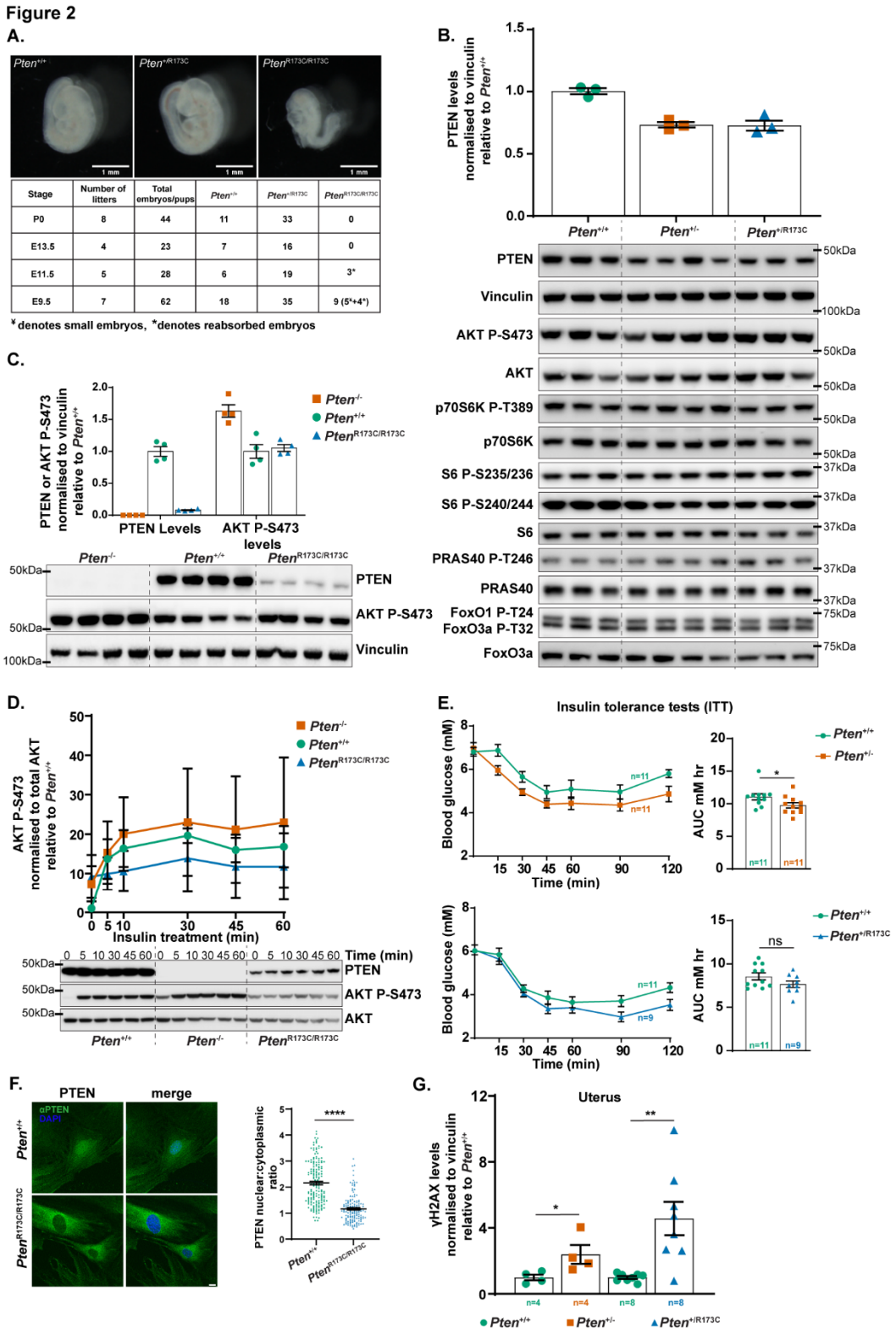

Figure 2. Characterisation of *Pten*$^{+/R173C}$ mice. (**A**) Homozygous *Pten*$^{R173C/R173C}$ mice die *in utero* after embryonic stage E9.5. Images show morphology of E9.5 *Pten*$^{+/+}$, *Pten*$^{+/R173C}$ and *Pten*$^{R173C/R173C}$ embryos. Scale bar: 1 mm. The table shows the number of embryos/pups of each genotype obtained at the indicated time points. ¥ indicates embryos smaller in size and * indicates embryos that had been reabsorbed. (**B, C**) Protein extracts from MEFs of the indicated genotype were used for immunoblotting with the antibodies shown. Data shown as mean ± SEM. At least 3 independent MEF lines of each were used for (B) and 2 independent MEF lines were used for (C). (**D**) MEFs of the

1129 indicated genotype were treated with insulin (100 nM) for the indicated times and protein extracts
1130 immunoblotted with the antibodies shown. Data shown as mean ± SEM from 2 independent MEF lines
1131 for each genotype. (**E**) ITT assays on 3-month-old male mice of the indicated genotypes. XY curves
1132 show blood glucose levels post insulin injection over time. Bar graphs show mean ± SEM of
1133 measurements of Area Under the Curve (AUC). Statistical analysis performed using Unpaired Student's
1134 t-test. (**F**) MEFs of the indicated genotype were immunostained with antibodies to PTEN (green) and
1135 DAPI (blue) and imaged by confocal microscopy. Scale bar: 10 µm. Graphs show nuclear:cytoplasmic
1136 ratio of the GFP MFI (mean ± SEM from 3 independent experiments). Statistical analysis was performed
1137 using Unpaired Student's t-test. (**G**) 6-week-old mice of the indicated genotypes were treated with
1138 7Gy γ-radiation and protein extracts from uterus were used for immunoblotting. Graph shows levels
1139 of γH2AX relative to littermate *Pten*$^{+/+}$ controls. Data shown as mean ± SEM. Statistical analysis was
1140 performed using Mann–Whitney U tests. Accompanying immunoblots are shown in **Fig. S9A**. p-values
1141 for all statistical analysis: *, $p < 0.05$; **, $p<0.01$; ***, $p<0.001$; ****, $p<0.0001$. Mice used for
1142 generating MEF lines in (A-D and F) and for experiments in (E and G) were on a C57BL/6J background.

Figure 3

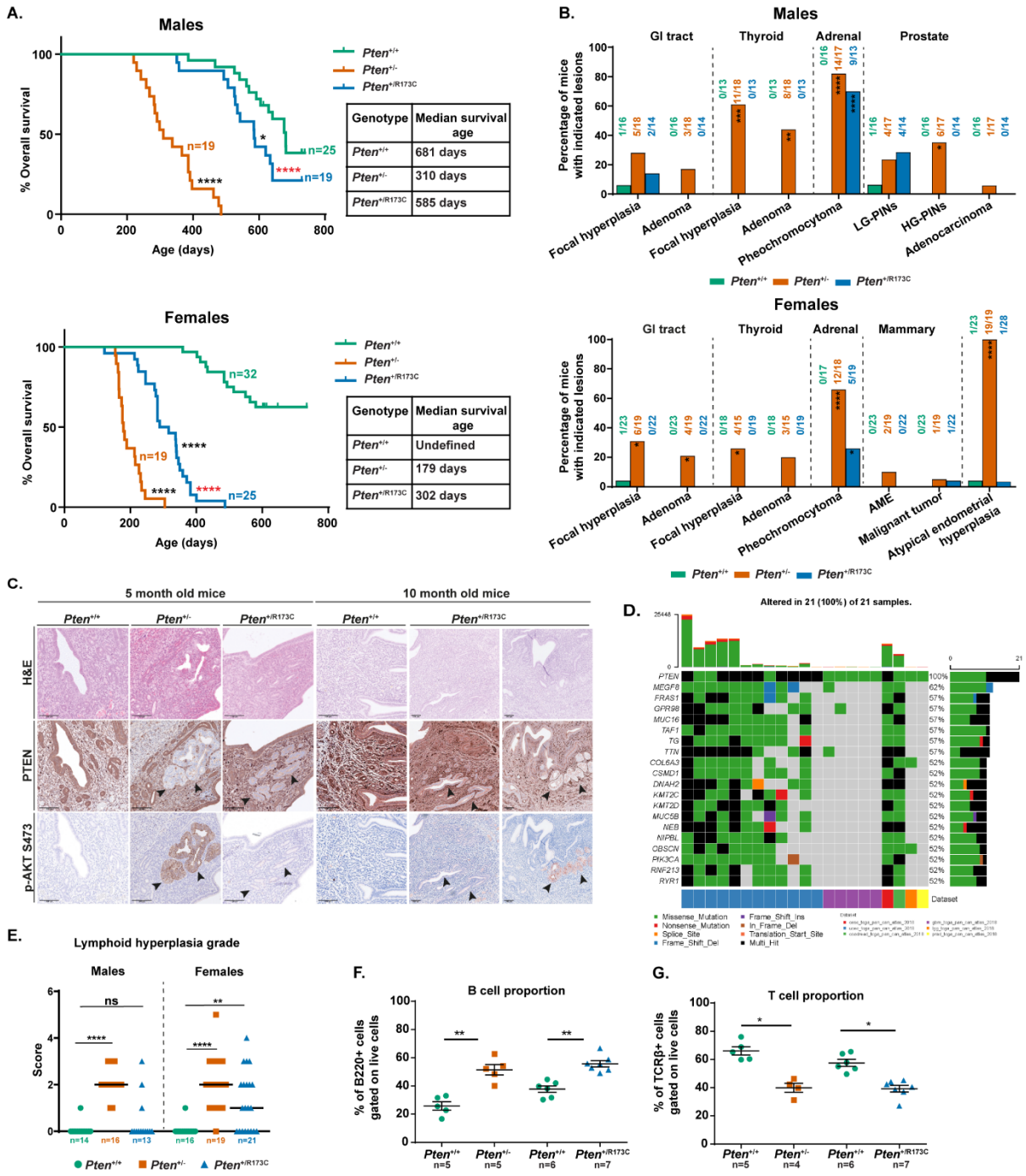

Figure 3. Survival and histopathological analysis of *Pten*$^{+/R173C}$ mice. *Pten*$^{+/R173C}$ and *Pten*$^{+/-}$ mice on a mixed C57BL/6J x Sv129 background were allowed to age. Mice were euthanized for welfare reasons (ill health or palpable masses with a combined size of ≥ 1.4 cm^2 surface area) or at a specified age. (**A**) Kaplan–Meier survival curves for male and female mice. Statistical analysis was performed using Log-rank (Mantel–Cox) test and Gehan–Breslow–Wilcoxon test. Comparisons were made to *Pten*$^{+/+}$ mice (p-values shown as black stars) or *Pten*$^{+/-}$ mice (p-values shown as red stars). Table show median survival age of the mice. (**B**) Incidence of specific tumour types in male and female mice, as assessed by histopathological analysis on all mice. Statistical analysis was performed using Fisher's exact test. (**C**) Representative IHC images of uteri from female *Pten*$^{+/R173C}$ and *Pten*$^{+/-}$ and littermate *Pten*$^{+/+}$ controls at the indicated timepoints, black arrowheads indicate loss of PTEN immunoreactivity and the corresponding AKT P-S473 immunoreactivity. (**D**) Oncoplot showing co-occurrence of mutations in the

1156 indicated genes in tumor samples harbouring PTEN-R173C mutation (cBioportal). (**E**) Grade of
1157 lymphoid hyperplasia in mice at the end of study. Graph shows scatter plot of scores from individual
1158 mice with line at median score. Statistical analysis was performed using Fisher's exact test. (**F-G**) Flow
1159 cytometry analysis was performed on the lymph nodes of female *Pten*$^{+/R173C}$, *Pten*$^{+/-}$ and littermate
1160 *Pten*$^{+/+}$ controls at 5 and 10 months of age. Graphs show the proportion of (F) B220+ B-cells and (G)
1161 TCRβ+ T-cells. Statistical analysis was performed using Mann–Whitney U test. p-values for all statistical
1162 analysis: *, $p< 0.05$; **, $p<0.01$; ***, $p<0.001$; ****, $p<0.0001$.

Figure 4

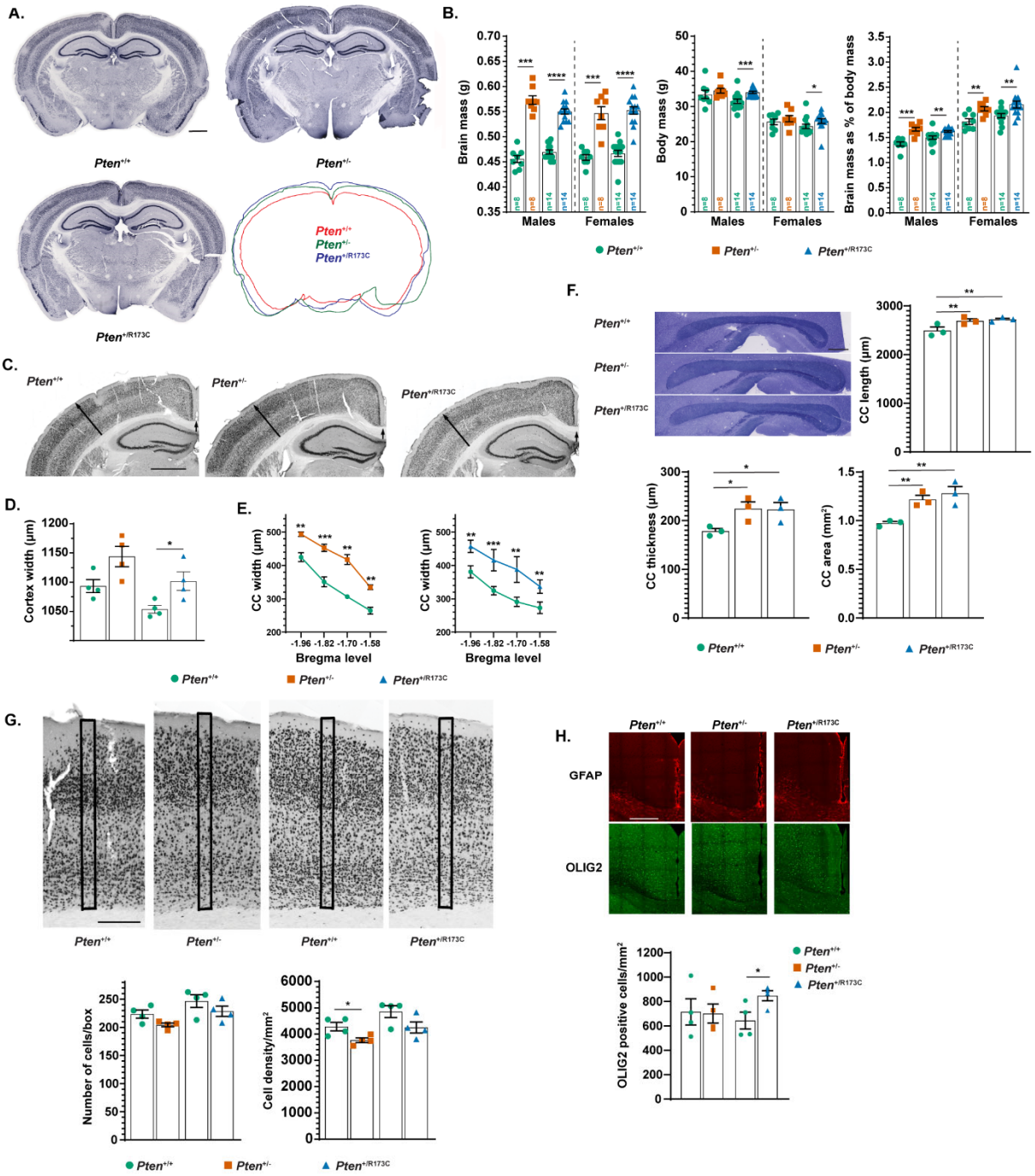

Figure 4. Enlarged brain phenotype with associated increases in grey and white matter areas in *Pten* mutant mice. (**A**) Representative NeuN immunostaining of coronal sections from *Pten*$^{+/+}$ and mutant animals at 3 months. The overlay of the contours of the depicted slices is also shown. Scale bar: 1000 µm. (**B**) Brain mass, body mass and brain mass as a % of body mass for male and female *Pten*$^{+/-}$, *Pten*$^{+/R173C}$ and WT littermate controls at 3 months. Data show mean ± SEM, statistical analysis performed using Two-tailed Mann-Whitney U test. (**C**) Representative NeuN immunostaining from coronal sections of WT and mutant animals at 3 months. Scale bar: 1000 µm. (**D**) Quantification of cortical thickness in the primary somatosensory cortex barrel field (area indicated with long arrows in C). n = 4 mice of each sex and genotype. Data show mean ± SEM, statistical analysis performed using Two-tailed Unpaired Student's t-test. (**E**) Quantification of the thickness of the corpus callosum at the indicated Bregma levels (area indicated with short arrows in C). n=4 mice of each sex and genotype.

1176 Data show mean ± SEM, statistical analysis performed using Two-way RM ANOVA with uncorrected
1177 Fisher's LSD test. (**F**) Representative sagittal sections from control and mutant mouse brains stained
1178 with Toluidine Blue and quantification of the corpus callosum length, thickness, and area. Scale bar:
1179 500 µm. n=3 mice per genotype. Data show mean ± SEM, statistical analysis performed using One-way
1180 RM ANOVA with uncorrected Fisher's LSD test. (**G**) Top: Representative images of coronal sections
1181 from the somatosensory cortex of *Pten*$^{+/+}$ and mutant animals at 3 months stained for NeuN. Scale bar:
1182 250 µm. Bottom: Quantification of the number and density of neurons in the indicated boxed areas in
1183 (G). n=4 mice of each sex each genotype. Data show mean ± SEM; statistical analysis performed using
1184 Two-tailed Unpaired Student's t-test. (**H**) Top: Representative images of sections from *Pten*$^{+/+}$ and *Pten*
1185 mutant animals at 3 months immunostained with OLIG2 and GFAP, Scale bar: 100 µm, and bottom:
1186 quantification of OLIG2 positive cells in the motor cortex. n=4 mice per genotype. Data show mean ±
1187 SEM and statistical analysis performed using Two-tailed Unpaired Student's t-test. p-values for all
1188 statistical tests: *, $p<0.05$; **, $p<0.01$; ***, $p<0.001$; ****, $p<0.0001$. Mice used were on a mixed
1189 C57BL/6J x Sv129 background.

Figure 5

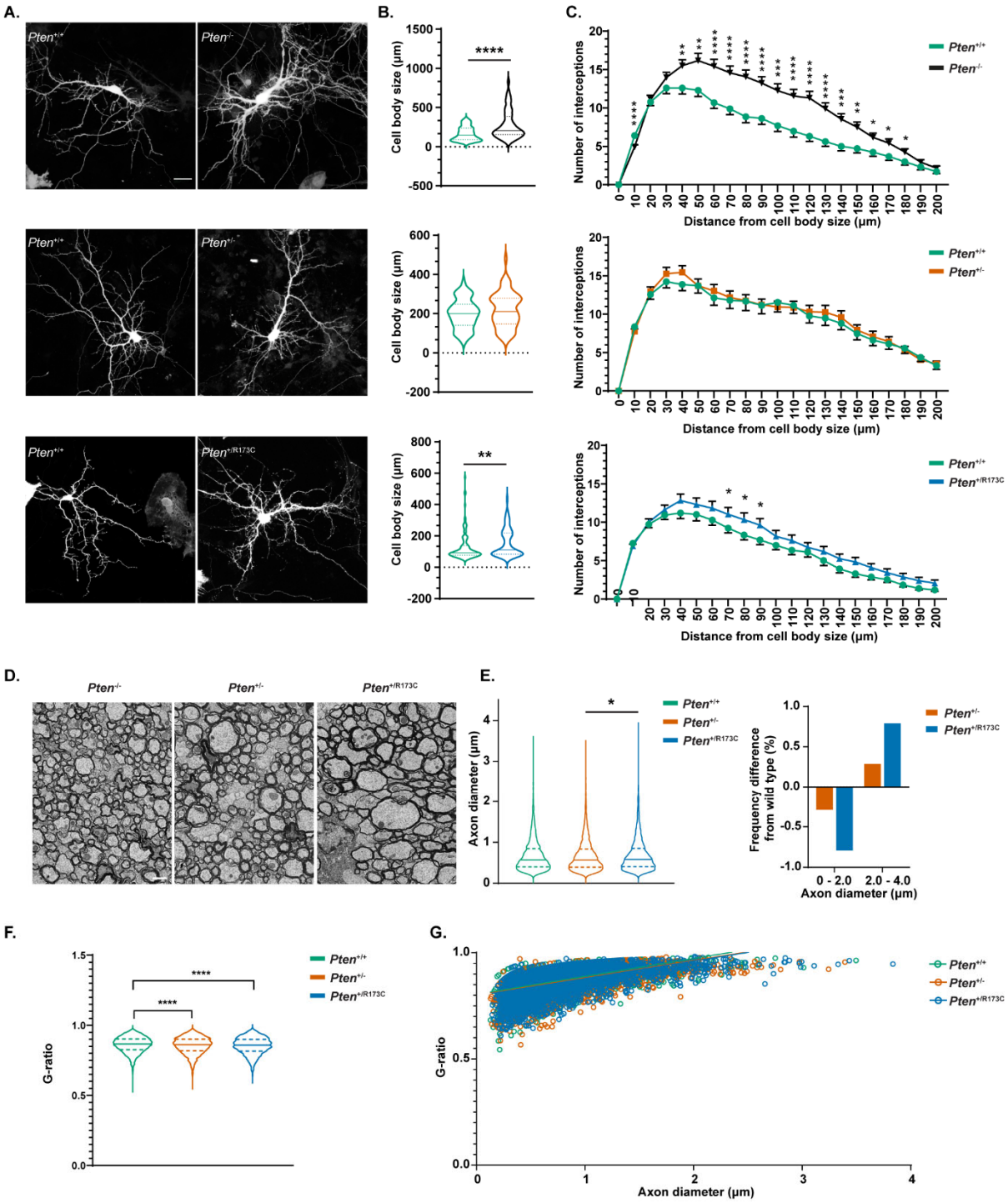

Figure 5. Neuronal and glial deficits in *Pten*$^{+/R173C}$ and *Pten*$^{+/-}$ mice. (**A**) Representative images from GFP-transfected cortico-hippocampal neurons prepared from the indicated *Pten* mutants and their respective *Pten*$^{+/+}$ littermate controls at DIV12/13. Neurons were stained for GFP. Scale bar: 20 µm. (**B**) Quantification of cell body size of GFP-transfected cultured cortico-hippocampal neurons shown in (A). from n>60 cells for each genotype from 3-6 independent experiments. Violin plots show mean ± SEM, statistical analysis performed using Two-tailed Mann-Whitney U test. (**C**) Sholl analysis of GFP-transfected cortico-hippocampal neurons shown in (A) from n=63–122 cells from 3–5 independent experiments. Data show mean ± SEM, statistical analysis performed using Two-way RM ANOVA with uncorrected Fisher's LSD test. (**D**) Representative electron micrographs of the corpus callosum in cross-sections from 3-month-old *Pten*$^{+/+}$, *Pten*$^{+/-}$ and *Pten*$^{+/R173C}$ mice. Scale bar: 1 µm. (**E**) Quantification of axonal dimeters and their frequency difference in mutant mice compared to *Pten*$^{+/+}$ littermate

1202 controls. >4500 axons measured in each of three mice per genotype. Violin plots indicate mean ± SEM,
1203 statistical analysis performed using Two-tailed Mann-Whitney U test. (**F**) Quantification of g-ratios for
1204 corpus callosum axons. >4500 axons measured in each of three mice per genotype. Statistical analysis
1205 performed using Two-tailed Mann-Whitney U test. (**G**) Scatter plot of g-ratios as a function of axon
1206 diameter in 3-month-old *Pten*$^{+/+}$, *Pten*$^{+/-}$ and *Pten*$^{+/R173C}$ mice. >4500 axons measured in each of three
1207 mice per genotype. p-values for all statistical tests: *, p< 0.05; **, p<0.01; ***, p<0.001; ****,
1208 p<0.0001. Mice used in (A-C) were on a C57BL/6J background, and in (D-G) were on a mixed C57BL/6J
1209 x Sv129 background.
1210